



Buckley, R., Kontoe, S., Jardine, R., Barbosa, P. and Schroeder, F. (2020) Pile driveability in low-to-medium density chalk. *Canadian Geotechnical Journal*, (doi: [10.1139/cgj-2019-0703](https://doi.org/10.1139/cgj-2019-0703))

There may be differences between this version and the published version. You are advised to consult the publisher's version if you wish to cite from it.

<http://eprints.gla.ac.uk/229113/>

Deposited on 25 January 2021

Enlighten – Research publications by members of the University of Glasgow  
<http://eprints.gla.ac.uk>

# Pile driveability in low-to-medium density chalk

Buckley, R.M.<sup>1</sup>, roisin.buckley@eng.ox.ac.uk

Kontoe, S.<sup>2</sup>,

Jardine, R.J.<sup>2</sup>,

Barbosa, P.<sup>3</sup>

Schroeder, F.C.<sup>4</sup>

1. Department of Engineering Science, Oxford University 2. Department of Civil & Environmental Engineering, Imperial College London, 3. Iberdrola Renovables Offshore, Deutschland, Berlin, Germany 4. Geotechnical Consulting Group LLP, London, UK

(MAIN TEXT AROUND 7900 WORDS)

## ABSTRACT

---

Pile driving in low to medium density chalk is subject to significant uncertainty. Predictions of Chalk Resistance to Driving (CRD) often vary considerably from field driving behaviour, with both pile refusals and free falls under zero load being reported. However, recent field studies have led to better understanding of the processes which control the wide range of behaviour seen in the field. This paper describes the primary outcomes of the analysis of dynamic tests at an onshore and an offshore site and uses the results to propose a new method to predict CRD. The method is based on phenomena identified experimentally: the relationship between cone penetration resistance and CRD, the attenuation of local stresses as driving advances and the operational effective stress interface shear failure characteristics. The proposed method is evaluated through back analyses of driving records from independent pile installation cases that were not included in developing the method, but involved known ground conditions, hammer characteristics and applied energies. The proposed method is shown to lead to more reliable predictions of CRD than the approaches currently applied by industry.

*Keywords:* chalk, piles, driveability

## 1 INTRODUCTION

---

2 Pile driveability analyses are commonly used to assess the sizes and types of hammer required to drive  
3 piles to target depths in given soil or rock profiles, without generating excessive driving and fatigue  
4 stresses. The analyses require the pile dimensions and estimates of the soil resistance to driving (SRD);  
5 the latter are usually made with empirical approaches. If instruments are placed near the pile head to  
6 measure strain and acceleration during driving hammer blows (see Figure 1a), dynamic back-analyses  
7 can be conducted to assess the SRD encountered in the field. Signal matching techniques ([Rausche et](#)  
8 [al., 1972](#)) utilising one-dimensional stress wave theory may be used to compute signals of either force,  
9  $F$ , or velocity times pile impedance,  $Z_v$ , which are matched with those measured at the pile head. The  
10 input parameters to the adopted soil resistance model, including SRD, are changed iteratively until a  
11 good quality match is obtained. The solutions are not unique and multiple approximations can be found  
12 that give similar fits to the measured signals, leading to potential bias in the results obtained by different  
13 operators, [see Fellenius \(1988\)](#) or [Buckley et al. \(2017\)](#). Pile driveability analysis can also be employed  
14 to back-analyse SRD using the hammer characteristics, driving records of transferred energy and blow  
15 counts as a reference (see Figure 1b) and utilising the same one-dimensional stress wave theory and soil  
16 resistance models. Methods for estimating the input SRD into these models in sands and clays, including  
17 those from [Toolan and Fox \(1977\)](#), [Stevens et al. \(1982\)](#) or [Alm and Hamre \(2002\)](#), have been derived  
18 empirically from driveability back-analyses. However, signal matching offers a more representative  
19 means of determining changes in pile capacity during pile installation than driveability back analyses  
20 since a single signal obtained during one blow is matched iteratively, as opposed to a driveability  
21 analysis, where the blow count profiles are produced for a given number of blows per penetration  
22 (Figure 1b).

23 A range of important oil, gas, offshore wind, port and transport structures are founded on piles driven  
24 in chalk over the large outcrops found in NW Europe (see [Jardine et al. \(2018\)](#)). However, there is no  
25 method currently available to predict the conditions applying to such piles during driving in chalk.  
26 Iberdrola have recently installed 2.7 to 3.7m diameter,  $D$ , open-ended tubular steel piles to support wind

turbine generator and offshore substation jacket structures at the Wiking Offshore Windfarm (OWF) in the Baltic Sea. The piles are founded in glacial till and low-medium density chalk. The windfarm pile installation followed a novel offshore static and dynamic pre-construction pile test programme on 1.37m diameter steel pipe piles ([Barbosa et al., 2015](#), [Buckley et al., 2020](#)), which formed the basis of an Innovate-UK supported Joint Industry Project between Iberdrola, Imperial College and the Geotechnical Consulting Group (GCG). The offshore tests were supplemented by further static, dynamic and cyclic tests in chalk at an onshore test site near St. Nicholas-at-Wade (SNW) in NE Kent, UK ([Buckley et al., 2018a](#), [Buckley et al., 2018b](#)). This paper proposes a preliminary CRD approach, for use in driveability predictions, which was developed from the static testing research at the latter two test sites, as well as signal matching studies on blows recorded over a wide range of pile scales and embedment depths. This paper gives first an overview of the characteristics of pile installation in chalk. A description of the test sites follows, along with observations made from the dynamic analyses undertaken at each site. The development of the proposed new method is then outlined before it is used to back calculate the hammer blows observed in installations for cases that were not included in the dataset from which the expressions were developed.

## PILE INSTALLATION IN CHALK

---

### *Stress changes during pile installation, equalisation and loading of piles in chalk*

Driving of open-ended steel piles in low-medium density chalk imposes cycles of high compressive stresses beneath the piles' annular base. These gradually de-structure the chalk as the tip advances towards, and eventually penetrates below, any given horizon in the chalk profile ([Buckley et al., 2018b](#)). It is well-known that local pile shaft stresses tend to rise and fall in clays and sands, in keeping with local density or shear strength variations, and also degrade with increasing relative pile tip depth,  $h$ , as the pile penetrates ([see Heerema, 1978](#)). The local shaft stresses developed in chalk also reflect the cone penetration test (CPT) profile trends, but (as shown later) reduce far more markedly with increasing  $h$  than in clays or sands ([Buckley et al., 2018a](#)). This may explain the very low driving resistances (0-20kPa) and free-falls or pile "runs" under self-weight that have been reported from the field ([e.g.](#)

[Carotenuto et al., 2018](#)). Driven pile installation in chalk may be partially drained, with consolidation occurring during driving and potentially progressing significantly before the end of installation, leading to water content reductions in the chalk immediately surrounding the pile shaft. Driving records also indicate that shaft capacity gains, or set-up, often develop during driving pauses; the shaft capacities of large piles driven offshore are thought to double in as little as 10 minutes ([Buckley et al., 2020](#)). Static and dynamic tests on aged piles have shown five-fold shaft capacity increases for large offshore driven piles when tested three to four months after driving and after 8 months with smaller piles driven above the water table at onshore test sites ([Buckley et al., 2018b](#)). Similar shaft capacity increases were obtained at the same site by ([Ciavaglia et al., 2017](#)).

Key aspects of the fundamental processes associated with the above phenomena are illustrated schematically in Figure 1. Here the effective stress states, experienced by chalk elements, located initially under the pile tip's annulus during pile installation, are considered at a depth  $z$  below ground level. Four stress states are illustrated, where: (A) the pile tip is above  $z$ , (B) the pile tip has just arrived at  $z$  (C) the pile tip is below  $z$  at the end of installation and (D) the pile tip is at  $z$  at the end of the equalisation period. The effective stress states applying at depth  $z$  at each stage are shown in specific volume,  $v$  – mean effective stress,  $p'$ , space on Figure 2, following [Buckley \(2018\)](#). Prior to the pile reaching depth  $z$ , elements are at the *in-situ* stress state, where the mean effective stresses,  $p'$  are relatively low (zone A). When the tip reaches depth  $z$ , the element below experiences a sharp increase in mean effective stress, following Path (A-B), assuming initially undrained conditions. The natural cemented structure allows states that exist to the right of the critical state line (zone B) until large straining causes the chalk to lose its natural structure and tend to a weak puttyfied state; generating high pore-water pressures (zone C). However, the radial effective stresses generated on the driven pile shafts subsequently increase during the equalisation period resulting in the Path C-D, through mechanisms that potentially include radial stress re-distribution, putty reconsolidation and corrosion/physio-chemical processes involving the pile and chalk.

#### *Prediction of installation stresses*

The SRD for a fully coring open-ended pile is given by:

$$SRD = \pi \left( D \int_0^{L_p} \tau_{fi} dz \right) + A_{ann} q_{ba} \quad 1$$

Where,  $\tau_{fi}$  is the total (internal and external) shaft resistance during driving,  $L_p$  is the pile embedment,  $A_{ann}$  is the annular steel area and  $q_{ba}$  is the end-bearing applying on the steel annulus. Methods available to estimate SRD during pile installation in sands include the [Alm and Hamre \(2002\)](#) approach which accounts for length effects as a function of the net CPT cone resistance,  $q_t$ , the relative distance of a given soil horizon above the pile tip  $h$ , the ultimate interface shearing angle,  $\delta'_{ult}$  and the effective overburden pressure,  $\sigma'_{vo}$ .

$$\tau_{fi} = f_{sres} + (f_{si} - f_{sres}) e^{-\frac{\sqrt{q_t}}{80 \sigma'_{vo} h}} \quad f_{si} = 0.0132 q_t \left( \frac{\sigma'_{vo}}{p_a} \right)^{0.13} \tan \delta'_{ult} \quad f_{sres} = 0.2 f_{si} \quad 2$$

where  $p_a$  is the atmospheric pressure. For base capacity, the [Alm and Hamre \(2002\)](#) formulation suggests  $q_{ba} = 0.15 q_t (q_t / \sigma'_{vo})^{0.2}$  in sands accounting for the lower pile tip displacements and capacity induced during a hammer blow rather than during static failure. The long-term static pile capacity differs from that at the End of Driving (EOD), due to effects of equalisation, ageing, consolidation and different levels of ultimate pile tip movement. However CPT-based design methods for sand such as ICP- ([Jardine et al., 2005](#)) and UWA-05 ([Lehane et al., 2005](#)) that were developed to represent medium-term equalised capacity, have been used to predict SRD in driveability studies with some success ([Byrne et al., 2012](#), [Schneider and Harmon, 2010](#)). [Rimoy et al. \(2015\)](#) argue that end of installation shaft capacities amount to around two thirds of the ICP-05 sand predictions. Post driving ageing processes allow the shaft resistances to rise and match the ICP-05 capacities within perhaps two weeks after of driving. They continue to operate and within one year may allow piles to reach final shaft capacities more than double the ICP-05 values.

There is currently no industry-standard method available to predict the driving stresses applying during installation for pre-formed steel piles driven in chalk. However, use is often made of the CIRIA C574 design guidelines for static capacity in chalk ([Lord et al., 2002](#)), which recommend adopting an ultimate limiting shaft resistance of 20kPa in low-medium density material and 120kPa in all other grades and a base capacity that depends on the standard penetration test (SPT)  $N$  value. Recently, [Dührkop et al. \(2017\)](#) presented a method to predict CRD based on the back analysis of offshore driving records.

Different values of unit shaft resistance and end bearing were applied that depend on the intact dry density (IDD) of the chalk. The effect of increasing pile penetration on lowering the CRD was partly accounted for by assigning higher values of values of  $\tau_{fi}$  and  $q_{ba}$  at the bottom of each layer, although this introduces inconsistency into the model when the pile tip penetrates a layer without reaching the base. [Dührkop et al. \(2017\)](#) recommend increasing shaft CRD by a factor of three, over a distance of 0.5m above the pile tip, to account for the rapid and significant set-up which was observed during operational pauses in driving.

The method proposed in this paper uses an effective stress-based approach to predict driving radial effective stresses based on the key phenomena identified by [Buckley et al. \(2018b\)](#) and [Buckley et al. \(2018a\)](#) namely (i) the ability of CPT cone resistance to identify local variations in chalk properties (ii) the marked effect of  $h$  on local stress attenuation and (iii) the interface effective stress shear failure characteristics.

## DESCRIPTION OF TEST SITES AND TESTING PROGRAMMES

---

### *Wikingen OWF*

[Buckley et al. \(2020\)](#) give a detailed account of the ground conditions encountered at the Wikingen OWF site located in the German Baltic Sea as indicated in Figure 3. Pleistocene glacial till deposits are found beneath thin Holocene layers and low-medium density Maastrichtian chalk is encountered beneath the tills. Bands that manifest high to very high-density chalk (or Danian Limestone) in layers of several metres thickness were also encountered at several of the 70 wind-turbine locations. The glacial till classifies as silty sand and sandy silt. Fluvio-glacial channels are incised into the chalk at discrete locations, infilled with material that classifies as a sandy silt/silty clay. The Wikingen chalk classifies as a structured Grade A1/A2 material. It has low-medium density (IDD generally  $<1.5\text{Mg/m}^3$ ), is extremely weak and has closely spaced, closed or clean fractures ([Bowden et al., 2002](#)) with occasional flint bands and nodules. The Unconfined Compressive Strength (UCS)  $q_u$  values range from 0.2-0.8MPa, falling below published onshore UK trends ([Matthews and Clayton, 1993](#)). Figure 4 shows a typical CPT profile. The glacial tills generally show  $q_t$  of 3-30MPa, with peaks up to 50MPa in isolated

thin dense sand layers and sleeve frictions of 100-400kPa. Excess penetration pore pressures, measured at the  $u_2$  position, showed generally negative values (-100 to -250kPa) with discrete peaks up to +1MPa. The  $q_t$  profiles in the chalk were averaged over 0.3m penetration intervals, following [Smith \(2001\)](#), generally giving 10-20MPa in the structured chalk, and peaks up to 60MPa. Sleeve frictions,  $f_s$ , were 200-400kPa, while  $u_2$  values were up to 10MPa at 30m below seabed.

Noting the known effects of pile driving, [Doughty et al. \(2018\)](#) explored the Wikingers chalk's properties when de-structured by undrained heavy compaction and performed undrained triaxial compression tests on aged and unaged samples. Consolidation of the de-structured samples resulted in initially denser-than-critical states which tended to initially contract and then dilate strongly when taken to large shear strains. Laboratory interface ring shear tests conducted by [Fugro \(2013\)](#) with mild steel interfaces having similar average roughnesses to driven steel piles ( $R_a \approx 10\text{-}15\mu\text{m}$ ) and under field normal effective stress levels (100-300kPa) gave  $\delta'_{ult}$  angles of 32-34°. The latter values are consistent with those reported by others at similar stress levels; [Le et al. \(2014\)](#), [Ziogos et al. \(2017\)](#).

Pile testing advanced at Wikingers in two phases. The pile types and details included in this study are summarised in Table 1. The first 'pre-construction' piling campaign involved three locations where three 1.37m outside diameter steel tubular piles were driven using a Menck MHU 800S hammer. At each location, pile 1 was subjected to dynamic testing only, pile 2 was subjected to a static tension test and pile 3 was an un-failed reaction pile. Strain gauges and accelerometers were attached to piles 1 and 2. The second phase of testing involved instrumented dynamic driving of 2.7 to 3.7m diameter tubular steel production piles. [Barbosa et al. \(2015\)](#) discussed the systems developed to meet the challenges of conducting the first remotely-controlled, full-scale, seabed offshore load tests, while [Buckley et al. \(2020\)](#) give a detailed account of the entire Wikingers testing programme.

#### *St Nicholas at-Wade (SNW) test site*

The SNW test site is located in a chalk quarry approximately 15km west of Margate in NE Kent, UK (Figure 3). Low-medium density chalk is encountered from the surface. Within the depth range of interest the chalk fractures are spaced between 60 and 600mm and are generally open with discontinuity



apertures of <3mm (Grade B2/B3). Representative CPT profiles are provided on Figure 5. Cone resistances are similar to Wikingen, lying between 10 and 20MPa, while sleeve friction,  $f_s$  lies between 100 and 300kPa. Thin discrete and discontinuous flints were also encountered which gave sharp local peaks in  $q_t$  up to 60MPa. The penetration pore pressures reach 10MPa at the  $u_t$  (tip) position and 6MPa at the  $u_2$  (shoulder) position. Bishop interface ring shear tests by [Chan et al. \(2019\)](#) demonstrated that  $\delta'_{ult}$  ranged from 31.6° to 32.8° under 200kPa normal stress levels.

The piles of interest in this study were 139mm OD open-ended steel tubular piles (Table 1). The piles were monitored dynamically during driving with strain gauges and accelerometers fitted near the pile head and were subjected to axial static and cyclic loading after installation; [Buckley et al. \(2018b\)](#).

Table 1 Details of the pile diameters and pile penetrations used in this study

Location	Piles	Test site	Steel grade	D (m)	L <sub>p</sub> (m)	L <sub>p,chk</sub> (m)	D/t <sub>w</sub>
WK70	70-1, 70-2	Wikingen (pre-construction)	S355	1.37	30.7	24.2	34
WK43	43-1, 43-2	Wikingen (pre-construction)	S355	1.37	30.7	20.4	34
OSS	OSS-C2, OSS-C4	Wikingen (production)	S355	3.67	46.3	36.0	61
WK WTG	WTG-A	Wikingen (production)	S355	2.70	31.1	14.6	67
DP1	-	St Nicholas-at-Wade	L80/L90	0.139	5.5	5.5	16
DP4	-	St Nicholas-at-Wade	L80/L90	0.139	5.5	5.5	16
DP7	-	St Nicholas-at-Wade	L80/L90	0.139	5.5	5.5	16

## SIGNAL MATCHING METHODOLOGY

### Soil reaction models

Smith's (1962) approach to modelling pile driving base and shaft resistances remains the most commonly employed tool for practical drivability and signal matching analyses. Linear springs represent the relative movement between the pile and soil at each node along the discretised pile length (Figure 6) and these govern up to the point where a plastic slider allows slip, while a viscous dashpot represents all soil damping effects. The shear stress,  $\tau$  along the pile shaft is given by:

$$\tau = \min\left(\frac{w}{U_{q,s}}, 1\right) (1 + J_s v) \tau_s \quad 3$$

Where,  $U_{q,s}$  is the shaft soil “quake” or displacement required to mobilise the static shaft resistance,  $\tau_s$ ,  $w$  is the displacement,  $v$  is the velocity, and  $J_s$  is a shaft damping parameter (in s/m). Base resistance is represented in a similar manner to (3). Static shaft and base resistances are assessed based on the soil conditions. Values of quake and damping, analysed from driving records and comparable static tests, lie within a relatively narrow range; typical values for clays and sands are given in Table 2.

Table 2 Quake and damping parameters used in the drivability analysis ([Alm and Hamre, 2002](#))

Pile	Shaft		Toe	
	$U_{q,s}$ (mm)	$J_s$ (s/m)	$U_{q,b}$ (mm)	$J_b$ (s/m)
Sand	2.5	0.25	2.5	0.5
Clay	2.5	0.25	2.5	0.5

Laboratory tests have shown non-linear relationships between soil strength and velocity ([Coyle and Gibson, 1970](#), [Dayal and Allen, 1975](#), [Litkouthi and Poskitt, 1980](#)) and a power law relationship may be adopted in place of (3) to reflect this dependency:

$$\tau = \min\left(\frac{w}{U_{q,s}}, 1\right) (1 + J'_s v^{\beta_s}) \tau_s \quad 4$$

Where  $J'_s$  and  $\beta_s$  are viscosity parameters. [Randolph \(2008\)](#) recommends adopting  $\beta_s = 0.2$ , and  $J'_s$  of 0 for a dry sand and 1 or higher for clay soils. The dynamic part of this model does not explicitly consider the effects of radiation damping in the far-field or differentiate between behaviour before and after pile slip. The dynamic shaft resistance is input as a proportion of the static shaft resistance and the internal shaft resistance is not considered separately to the external resistance.

Several rheological models have been proposed to better simulate the mechanics of pile driving (e.g. [Deeks and Randolph, 1995](#), [Holeyman, 1985](#), [Randolph and Simons, 1986](#), [Salgado et al., 2015](#)). The signal matching described in this study employed the research-oriented software IMPACT ([Randolph, 2008](#)) which utilises the method of characteristics ([De Josselin de Jong, 1956](#)) as a numerical method along with the [Randolph and Simons \(1986\)](#) resistance model for the shaft and the [Deeks and Randolph \(1995\)](#) model at the base. The shaft model (Figure 7) consists of a spring and radiation dashpot

connected in parallel, which represent the far-field response, connected in series to a plastic slider and a viscous dashpot which model the shear band around the shaft, subjected to viscous rate effects. The model equations are summarised in Table 3.

Table 3 Summary of equations and parameters using [Simons and Randolph \(1985\)](#) and [Deeks and Randolph \(1995\)](#) models in IMPACT

	Equation	No.	Parameter
Shaft resistance	$\tau = k_s w + c_s v \leq \tau_s$	(5)	
Spring	$k_s = \frac{G}{D}$		G, D
Radiation dashpot	$c_s = \frac{G}{v_s} = \sqrt{G\rho_s}$		G, $\rho_s$
Viscous effects	$\tau_{inter} = \tau_s \left( 1 + \alpha_s \left( \frac{\Delta v}{v_0} \right)^{\beta_s} \right)$	(6)	$\alpha_s, \beta_s$
Total base resistance	$Q_b = K_b w + C_b v \leq q_{b,s}$	(7)	
Spring	$K_b = \frac{4GR}{(1-\nu)}$		G, D, $\nu$
Radiation dashpots	$C_b = \frac{3.2R^2}{(1-\nu)} \sqrt{G\rho_s}$		G, D, $\rho_s, \nu$
	$C_1 = \frac{3.2R^2}{(1-\nu)} \sqrt{G\rho_s}$		
Subsidiary mass	$m_0 = 0.16 \frac{4R^3 \rho_s}{(1-\nu)}$		D, $\rho_s, \nu$

Prior to slip, the far-field response is described by (5). Where  $\tau < \tau_s$ , the spring and radiation dashpot govern and the pile and soil move together. During soil slip,  $\tau > \tau_s$ , the spring/dashpot system is disconnected and the pile and soil displacements are calculated separately. The viscous dashpot augments the shear strength of the soil at this point to account for rate effects (see Equation 6 in Table 3). The interface strength,  $\tau_{inter}$  is a function of the pile and soil relative velocity,  $\Delta v$ , a normalising velocity,  $v_0$  ( $=1\text{m/s}$ ), and viscosity parameters  $\alpha_s$  and  $\beta_s$ . The soil displacements are calculated by solving Equation 5 in Table 3 with a fixed value of  $\tau_s$ . The condition for re-joining of the pile and the soil is when  $\tau$  calculated using soil displacement and pile velocity,  $\tau_{s,p} < \tau_s$  ([Randolph and Simons, 1986](#)). Open-ended steel pipe piles can mobilise shaft resistance along their internal and external shaft areas. [Randolph \(1987\)](#) introduced a separate model for the soil plug inside open-ended piles, which is implemented into IMPACT.

The [Deeks and Randolph \(1995\)](#) base model (Figure 7) is similar to the [Randolph and Simons \(1986\)](#) shaft model with the addition of two lumped masses, one connected to the pile node ( $m_0$ ) and one ( $m_1$ ) connected through a second radiation dashpot ( $C_1$ ). The spring and dashpot follow the [Lysmer and Richart \(1966\)](#) model, in which the response of a circular footing is given by (7 in Table 3. [Deeks and Randolph \(1995\)](#) found that for undrained conditions ( $\nu = 0.5$ ),  $m_1 = 0$  and the second radiation dashpot has no significant effect, while it would be possible to allow for viscous enhancement of the static end-bearing capacity, due to the high strain rates. [Randolph \(2008\)](#) notes that in clay soils, where viscous effects may be significant, the radiation damping is also high and dominates the soil response at the pile tip. IMPACT therefore currently makes no additional allowance for viscous effects at the base. While it is not possible to investigate the influence of viscous effects on base resistance, as mentioned later, signal matches conducted on adjacent piles at the same pile age as tension static load tests show good correlation outcomes, which gives confidence in this approach ([Buckley et al., 2020](#))

#### Input parameters

The input parameters required for IMPACT analyses, summarised in Table 4, are predominantly linked to measurable soil properties. The soil density,  $\rho_s$  and shear moduli,  $G$ , taken for the cases considered below were determined from local site investigations. Operational secant stiffnesses,  $G_1$  were scaled down from the measured small-strain,  $G_{max}$  values to account for soil non-linearity as recommended by [Alves et al. \(2009\)](#) and [Salgado et al. \(2015\)](#). The best matches for the Wikingers glacial till were obtained taking  $G_1 = 200\sigma'_{vo}$  following [Lee et al. \(1988\)](#) for sandy soils, which resulted in  $G_1/G_{max}$  ratios of  $< 0.3$ , while  $G_1 < 0.2G_{max}$  was assumed to model the Wikingers and SNW chalks.

Table 4 Summary of signal matching input parameters in IMPACT at EOD, BOR and, prior to and following a driving pause

	Fixed parameters						Varied parameters	
	$\rho$ (g/cm <sup>3</sup> )	$G_1$	$\alpha_s$	$\beta_s$	$\nu$	Ratio inner/outer	$q_{ba}/q_{t,1.5D}$	$\tau_s$
Wikingers - glacial till	1.94	$200\sigma'_{vo}$	1.15	0.2	0.5	0	Varied	Varied
Wikingers - chalk	2.22	$< 0.2G_{max}$	1.00	0.2	0.5	0	Varied	Varied
SNW - chalk	1.94	$< 0.2G_{max}$	1.00	1.0	0.5	0.1 – 0.15	Varied	Varied

Consistent with Randolph's (2008) recommendations  $\beta_s$  was taken as 0.2 for the Wiking till and chalk. The specific  $\alpha_s$  parameter, which is shown later to have a strong influence on the result in "easy" driving cases, is known to be variable since it depends on the specific soil or rock state ([Biscontin and Pestana, 2001](#), [Brown and Hyde, 2008](#), [Triantafyllidis, 2001](#)). In the Wiking chalk,  $\alpha_s$  was taken as 1.1, based on the correlation of [Loukidis et al. \(2008\)](#) between  $\alpha_s$  and undrained shear strength  $s_u$  and assuming that the weak chalk putty annulus formed close to the shaft governs its resistance. For clays, [Brown and Powell \(2013\)](#) suggest a tentative relationship between  $\alpha$  value and plasticity index (PI) from rapid load tests which gives a range of 0.73-0.95 for the low plasticity glacial till at Wiking, where the PI is  $8.8 \pm 3.4$ . [Randolph \(1993\)](#) used an  $\alpha_s$  value of 1 for signal matches on piles driven in stiff low-plasticity glacial till at Tilbrook Grange. A slightly higher  $\alpha_s$  of 1.15 was used in the analyses for the glacial till at Wiking, which gave the best quality signal matches and closest correlation with static load tests conducted on adjacent piles at the same pile age ([Buckley et al., 2020](#)).

IMPACT treats the inside and outside shaft resistances as independent and good quality signal matches could only be obtained for Wiking by keeping the ratio of the independent internal to external shaft resistances, between 0 and 0.2. Open-ended tubular steel piles displace far lower volumes of soil and develop lower (base and shaft) resistances than closed-ended piles ([see e.g. Gavin and Lehane, 2007](#)). Experiments in sand ([Chow, 1997](#), [Jardine et al., 2005](#)) have shown that internal shaft resistance reduces dramatically as the internal diameter increases. Internal shaft resistance is likely to be relatively minor and concentrated towards the base of large-scale piles in sands. Recent field tests on instrumented 'double-wall' piles in gravelly sand by [Han et al. \(2019\)](#) confirmed that the internal resistance contributes a small proportion of the overall base resistance. Signal matching of the Wiking piles appears to indicate similar behaviour. The Wiking piles all drove in a fully coring mode; to simplify the analyses it was assumed that shaft resistance applied on only the external areas. The parameters chosen for Wiking were checked by comparing the shaft capacities determined from re-strike blows on aged piles with static tension tests conducted on adjacent piles at the same age ([Buckley et al., 2020](#)).

A similar  $\alpha_s=1$  viscosity term was adopted for SNW for which  $\beta_s$  was also taken as unity, reverting to the original Smith formulation, which trial and error calculations showed to be necessary to obtain fair

1 matches with the measured field records. The best quality signal matches were obtained at SNW by  
2 maintaining the ratio of internal to external shaft resistance between 0.1 and 0.15 for the relatively small  
3 diameter piles. Residual base stresses were neglected at both sites.

4 Only the base and shaft resistances were varied between EOD and BOR or prior to and following a  
5 driving pause (see Table 4), assuming that the degraded secant stiffnesses are unaffected by time over  
6 these strain ranges. An example signal match on a Wikinger pile is shown on Figure 8 in terms of the  
7 measured and back calculated  $F$  and  $Z_v$ , upward wave,  $F_{up}$ , where  $F_{up}=(F-Z_v)/2$ , and pile head  
8 displacement, obtained by double integration of the measured accelerations.

#### 9 *Sensitivity of signal matching to input parameters*

10 It is useful to consider the degree to which the signal matching analyses are sensitive to the primary  
11 model parameters ( $G$ ,  $\alpha_s$  and  $\beta_s$ ) before moving on to review specific back-analyses made for Wikinger  
12 and SNW. We explore these sensitivities below by considering example hammer blow records taken  
13 from the Wikinger field dataset.

14 The effect of varying the shear modulus from  $G_{max}$  to an operational value,  $G_I$  has been investigated for  
15 the two distinct cases covering: i) a low overall pile capacity, giving easy driving and ii) a high capacity,  
16 hard driving, blow. The pile head velocities for each case are shown in Figure 9. Where the overall  
17 capacity is high, the spring and radiation dashpot dominate the response over the main length of the  
18 hammer blow. Conversely, when the overall capacity is low, viscous effects dominate along the shaft  
19 and the spring and radiation dashpot are only activated towards the latter portion of the record.

20 Consider first the low pile capacity case, for which the slip condition is reached very quickly after  
21 applying each blow. The pile and soil become disconnected, their displacements are calculated  
22 separately, and the pile response is dominated by the viscous terms in (6). The pile and soil can only  
23 reconnect over the final stages of the movement induced by the blow, when the pile is almost at rest  
24 and the spring and dashpot are reactivated. When the viscous effects dominate, changes in  $G_{max}$  do not  
25 affect the upward wave (and therefore the resistance) and have little effect on the degree of the match  
26 between measured and computed  $F$  and  $Z_v$ , where  $\tau_{s,p} > \tau_s$  along the entire pile shaft. This is illustrated

in Figure 10 by showing the overall evolution of soil and pile displacements for one shaft element when  $G_I$  is taken as 10, 50 and 100% of  $G_{max}$ , corresponding to  $G_I/\tau_s$  ratios  $\approx 260$ , 1300 and 2650. While the soil displacements vary strongly with  $G$ , only the final portions of the pile displacements, recorded at the pile head, are affected and  $G$  only marginally influences the permanent displacement or set recorded as the pile comes to rest.

Consider next a hammer blow for a high overall capacity pile which provokes a stiffer initial spring and dashpot response and maintains  $\tau_{s,p} < \tau_s$  for the main part of the blow's signal duration. The spring and radiation dashpot are engaged for almost the whole blow duration and the response is governed by the soil's shear modulus and the soil density. Consequently, the upward wave signal is strongly affected by changes in  $G$ . The evolution of soil and pile displacements for this case are shown on Figure 11. Considerably less pile displacement is observed and the pile and soil displacements are both sensitive to variations in  $G$  over the full blow duration.

The easy driving blow was further used to demonstrate the effect of the viscosity parameters on the response during a blow. Values of  $\beta_s$  of 0.2, 0.3, 0.4 and 0.5 were considered taking  $\alpha_s=1$ . Values of  $\alpha_s$  of 0.3, 0.5, 1 and 1.5 have also been adopted, taking  $\beta_s=0.2$ . In this parametric investigation the stiffness was kept constant with  $G_I=10\% G_{max}$  ( $G/\tau_s \approx 260$ ). As  $\alpha_s$  and  $\beta_s$  decrease, the proportion  $\tau_{inter}/\tau_s$  decreases, which leads to a lower dynamic resistance at the interface. Figure 12 shows the effect of the viscosity parameters on  $F_{up}$  and the pile head displacement. Changes in  $\beta_s$  have little effect on  $F_{up}$  and on pile head displacement over the stage where the velocity is high, and the viscous effects calculated using (6) are known to reach a plateau ([Litkouthi and Poskitt, 1980](#)). As the velocity decreases towards the pile toe, the effect of increases in  $\beta_s$  on reducing  $F_{up}$  become clearer; see Figure 12(a), which is accompanied by a decrease in pile head displacement; Figure 12(b). Figure 12(c) shows the effect of a change in  $\alpha_s$  on  $F_{up}$  for the same hammer blow. Increases in  $\alpha_s$  affect the entire record, generating an increase in  $F_{up}$ . Figure 12(d) shows the corresponding effect on pile head displacement, which falls with increasing  $\alpha_s$ . When driving is easy, varying  $\alpha_s$  has a stronger influence on the interpreted SRD values than changing the shear modulus or the parameter  $\beta_s$ .

## BACK ANALYSIS OF PILE RESPONSE DURING DRIVING

---

The back analyses undertaken for blows recorded at different stages of pile installation at Wiking and SNW were central to deriving the preliminary new driveability approach for chalk. While the common practice in signal matching analysis is to examine only the EOD blow, cases were considered that covered blows applied after operational driving pauses and extended ageing periods, as well as continuous penetration for piles of different dimensions. These field records also demonstrated the fast potential rates of gains in capacity over time and the marked effect of pile relative tip depth,  $h$  on local shaft shear stress attenuation.

### *Pile response over operational pauses*

[Buckley et al. \(2020\)](#) describe the capacity increases with time observed during the static and dynamic tests at Wiking. The shaft resistance interpreted from dynamic tests,  $\tau_{s,d}$  in the chalk doubled within two minutes and re-doubled within 90 minutes tending to a long-term stable set-up factor of  $\approx 5.6$  after three to four months. Pauses in pile driving affect the  $F$  and  $Z_v$  signals measured during a dynamic test, as is demonstrated on Figure 13(a) at EOD and BOR on the same pile, 77 days after installation. A clear increase in the force trace is observed in the +77 day blow, along with a decrease in measured  $Z_v$  which indicates a significant increase in capacity over this time period. A similar trend for  $F_{up}$  to increase with time is observed over operational pauses in driving (Figure 13(b)).

Figure 14 shows, for a pile driven at Wiking location WK70-1, the shaft resistance back-analysed using IMPACT from the blow: (i) immediately prior to a pause in driving (412), (ii) immediately following an 8 minute long pause (413) and (iii) 2, 7, 17, 27 and 37 blows after the end of the pause, equivalent to further penetrations of 0.04, 0.15, 0.4, 0.7 and 1.0m. Again, only the shaft and base resistances were varied between the analyses. Shaft capacity can be seen to increase markedly over the 8 minute driving pause, indicated by the shaded portion in the figure, by factors of 1.2 in the glacial till and 2.0 in the chalk, while the base capacity was relatively unaffected. However, the capacity gains were lost rapidly after driving resumed and practically disappeared as the pile penetrated by a further 1m (0.73D) or  $\approx 30$  blows.



# Pile resistance at the end of installation

The EOD shaft resistance contributions developed in the soft superficial Holocene deposits appeared to be negligible at Wiking. The average driving shaft resistances  $\tau_{s,d}$  developed in the glacial till fell primarily between 30 and 200kPa and showed a clear tendency to reduce with  $h/R^*$ , where  $R^*$  is the equivalent radius  $(= R^2 - R_t^2)^{0.5})$  for the open-ended tubular piles. A similar, but far steeper, dependence on  $h/R^*$  was observed in the chalk with  $\tau_{s,d}$  values up to 300kPa observed close to the pile tip that reduce to minima as low as 10kPa as the tip advances. Figure 15 illustrates these trends for the WK70-2 location where a high to very high-density chalk (or Danian Limestone) layer also affected the driving records, giving EOD  $\tau_{s,d}$  values up to 50kPa between  $\approx 10$  and 15mbsb that fell outside the general trends for the lower density chalk. The EOD shaft and base stresses found by signal matching analyses for six large diameter Wiking test piles at an offshore substation (OSS) and wind-turbine (WK) locations are summarised in Table 5 along with the tests on three small piles (DP1, 4 and 7) driven at SNW. Fully continuous chalk CPT profiles were not available at all Wiking locations; where data was absent a local correlation between chalk  $q_t$  and shear wave velocity,  $V_s$  (obtained from borehole P-S logging) was employed (Buckley *et al.*, 2020). Where  $V_s$  was absent, a mean  $q_t$  profile from nearby locations with similar ground profiles was adopted.

Table 5 Pile capacities at the end of driving for all ten EoD tests

Pile	$\tau_{avg}$ (kPa) <sup>1</sup>	$q_{ba}$ (MPa)	$q_{ba}/q_{t,1.5D}$	$L_{p,chk}$ (m)
WK43-1	26 <sup>1</sup>	8.0	0.4	20.4
WK43-2	36 <sup>1</sup>	20.0	1.1	20.4
WK70-1	40 <sup>1</sup>	12.0	0.6	24.2
WK70- 2	35 <sup>1</sup>	7.0	0.4	24.2
OSS-C2	24 <sup>1</sup>	12.0	0.4	36.0
OSS-C4	29 <sup>1</sup>	6.0	0.2	36.0
WK WTG	30 <sup>1</sup>	15.0	0.8	14.6
SNW DP1	17	17.2	0.7	5.5
SNW DP4	15	12.1	0.7	5.5
SNW DP7	17	18.0	0.8	5.5

1. Along the whole pile length in glacial till and chalk

The average EOD shaft resistances  $\tau_{avg}$  reduced with increasing penetration into the chalk, with the 24kPa minimum for Wikingen corresponding to the OSS-C2 case for which  $L_{p,chl} = 36\text{m}$ . The SNW piles, which all penetrated by the same distance into the chalk-only profile, all gave  $\tau_{avg}$  less than 20kPa. At both sites the end bearing resistances interpreted from dynamic measurements made during continuous penetration were equivalent to base pressures around  $0.4$  to  $0.7q_{t,1.5D}$  (where  $q_t$  is averaged  $1.5D$  around the pile base) being mobilised over the open-ended steel piles' annular areas.

#### *Pile response to blows applied during main drive sections*

The relationship indicated in Figure 15 between the degree of penetration into chalk and the local shaft resistance was explored further by examining blows recorded at Wikingen during different driving stages. Noting first that highly instrumented ICP pile tests conducted at SNW ([Buckley et al. \(2018a\)](#)) showed that, as with clays and sands (see [Jardine et al. \(2005\)](#)), the local shaft stress can be described by a Coulomb law with:

$$\tau_{fi} = \sigma'_{ri} \tan \delta'_{ult} \quad 8$$

[Buckley et al. \(2018a\)](#) also found that the local radial effective stresses are related to the CPT cone resistance in a similar manner to that suggested for sands ([Chow, 1997](#), [Jardine et al., 2005](#), [Lehane et al., 1993](#)). Figure 16 employs these findings to interpret results from 10 blows recorded during continuous, uninterrupted pile driving stages for the largest, OSS, piles and four others recorded at wind-turbine locations at the Wikingen OWF site. Here the local  $\tau_{s,d}$  values derived from signal matching analyses over multiple shaft sections positioned in the chalk strata were each divided first by  $\tan \delta'_{ult}$  (with  $\delta'_{ult}=32^\circ$ ) to define the average radial effective stresses  $\sigma'_{ri}$  operating locally against each section of the pile shaft. The  $\sigma'_{ri}$  data were also normalised by the local corrected CPT tip resistance  $q_t$  to account for spatial variations in chalk conditions and plotted against the average relative tip depths  $h/R^*$  applying to the same shaft sections at the time of the blow. The  $h/R^*$  values considered ranged from 1.0 to 52.5.

Also shown are the trends interpreted from well-known design methods for piles driven in sands that incorporate an  $h/R^*$  dependency: the ICP-05 static capacity method ([Jardine et al., 2005](#)) and the SRD

approach of ([Alm and Hamre, 2002](#)), which were computed to correspond to the 40m long, 3.67m diameter, OSS piles assuming a constant  $q_t$  profile of 15MPa. The two sand methods show local stress reduction with  $h/R^*$  that is far less marked than that seen in the Wikingen chalk.

#### PROPOSED METHOD TO PREDICT CHALK RESISTANCE TO DRIVING

---

Following from the above discussion it is proposed that the local radial effective stresses developed by piles during driving in chalk may be related to local CPT cone resistance and  $h/R^*$  through Equation 9 in a similar manner to that applied previously for sands in the ICP-05 approach by [Jardine et al. \(2005\)](#).

$$\sigma'_{ri} = \zeta q_t \left( \frac{h}{R^*} \right)^{-\eta} \quad 9$$

Parameter  $\zeta$  reflects the radial effective stress reduction from a proportion of  $q_t$  immediately beneath the pile tip to the far lower ratio that operates on the lowest part of the shaft. The  $h/R^*$  term and exponent  $\eta$  account for the further reduction of radial effective stresses that takes place higher above the pile tip.

Figure 16 shows an interpreted power law trend between  $\sigma'_{ri}/q_t$  and  $h/R^*$  for the blows considered from the Wikingen dataset. Detailed inspection shows that the  $h/R^*$  dependency is most marked with the largest diameter (and largest  $D/t_w$  ratio) piles. It appears that the geometrical system applying in the field is not fully captured by the simple characterisation involving  $R^*$ , whose formulation includes the pile wall thickness.

As noted above the rates of degradation appear to increase with  $D/t_w$ . Figure 17 (a) plots the radial effective stresses interpreted as applying at the end of driving against  $h/R^*$ , as obtained from signal matching using IMPACT at all of the pile locations listed in Table 1; the 1.37m, 2.7 and 3.67m diameter piles installed at Wikingen and the 0.139m diameter piles installed at SNW. The power law relationship given in (9), is also shown where the parameter  $\zeta$  was adopted as 0.031 (indicative of a shear stress reduction behind the tip of  $\approx 5\% q_t$  for  $\delta'_{ult}$  of  $32^\circ$ ) and the parameter  $\eta$  was varied to achieve a reasonable match for each set of results. The chosen value of  $\zeta$  is of the same order as the radial stress reductions applying between the CPT tip and the friction sleeve, calculated using the CPT  $f_s/q_t$  ratios (which vary from  $\approx 1$  to 2%) and the interface shear angle applying between the CPT sleeve and the chalk,  $\delta'_{cpt}$  of

30.5°. The latter was measured in interface ring shear tests on stainless steel interfaces with similar roughnesses to cone sleeves; [Buckley et al. \(2018a\)](#). The resulting best fit for parameter  $\eta$  fell between 0.75 and 0.9. To obtain a single expression for  $\sigma'_{ri}$ , that covers a range of  $D/t_w$  values, it appears to be necessary to introduce a further geometrical factor into  $\eta$ . Figure 17 (b) plots the best fitting  $\eta$  parameters for the Figure 17 (a) cases against  $D/t_w$ . A power law relationship is fitted to the data which applies to piles with  $16 < D/t_w < 67$  during driving in low-to-medium density chalks that expands (9) as follows:

$$\sigma'_{ri} = 0.031q_t \left( \frac{h}{R^*} \right)^{-0.481} \left( \frac{D}{t_w} \right)^{0.145} \quad 10$$

where  $q_t$  is averaged over 300mm penetrations. A conservative lower limit to  $h/R^*$  was selected as 6 (reduced from the value of 8 used by [Jardine et al. \(2005\)](#)) to better replicate the shaft resistances observed in static and dynamic tests close to the pile base, although it is possible that a lower value may apply. Equation (10) is combined with (8) and (1) to predict shaft CRD for driveability assessments in low to medium density chalk, taking  $q_{ba}$  levels between 0.4 and 0.7 $q_t$  depending on the anticipated penetration per blow. Figure 18 plots the calculated profiles of shaft resistance obtained with the proposed method along with the measured values from the signal matching results at representative locations in Wiking and SNW. Pile WK43-1 and WK43-2 show different trends in shaft resistance, for identical piles driven <5m apart, illustrating the natural variations possible in material behaviour. Reasonable agreement is observed overall between the measured and calculated profiles of shaft shear stress over the majority of the pile shaft. The shear stress is less reliably predicted close to the pile base in several cases, which may be improved by further calibration of the rate dependent viscosity parameters in chalk and/or reducing the lower limit on  $h/R^*$ , as more data becomes available.

## DRIVEABILITY PREDICTIONS

---

The proposed method was checked by making hindcasts for pile driving blow counts recorded in chalk with other piles driven at the Wiking site and at another offshore windfarm with comparable chalk

strata, located in the Southern North Sea. The driveability predictions built on earlier work by [Norrie \(2015\)](#), [Ebensperger \(2017\)](#) and [Esper \(2017\)](#). The studies employed the Allwave-PDP software ([Allnamics, 2015](#)) which predicts pile driveability using one dimensional wave equation theory combined with the [Smith \(1962\)](#) soil resistance model (Figure 6). The driveability hindcasts employed:

1. Case records from each site that showed continuous driving with no operational pauses. One additional case where an operational pause occurred was considered;
2. Hammer characteristics that represented the equipment adopted for the pile driving with modifications that accounted for the actual input energy;
3. SRD contributions for any clay or sand layers derived by the [Alm and Hamre \(2002\)](#) method. The dynamic “Smith” model parameters used are given in Table 2;
4. Chalk CRD values found from the new approach as implemented into a beta (development) version of the Allwave-PDP program by [Middendorp \(2016\)](#). The base CRD was set equal to 0.4 times the cone resistance, at the lower end of the recommended range, which gave the most consistent results with the [Smith \(1962\)](#) soil resistance model;
5. The dynamic ‘sand’ parameters given in Table 2 were adopted for the chalk with a non-linear dependence of soil strength on pile velocity (4) through taking  $J'_s$  and  $\beta_s$  equal to 1 and 0.2 respectively. The latter were selected to be consistent with the signal matching analyses used to develop the new driveability method.

Figure 19 shows blow count profiles predicted by Allwave PDP profiles for piles that were driven at Wikingen, but not included in the method development described in the previous Section. As applied here, the new approach captures the blow count profiles for the 1.37m and 2.7m diameter piles installed at Wikingen with good accuracy. Figure 19 also shows, for reference, the blow counts predicted when CRD is set equal to the CIRIA constant 20kPa value. This approach, which is applied by many practitioners, leads to a less satisfactory overestimation of the blows recorded, particularly in the upper part of the chalk.

A case where an operational pause occurred was also considered, considering the installation of WK43-3 (Figure 19(c)) where driving paused for approximately 2 hours with the pile tip at 21mbsb. When

driving re-started, an almost threefold increase in blow counts was observed. A four-fold increase in shaft capacity over 3m (from 21 to 24m) was applied to the CRD which, when input into the model, captured the blow count response adequately. This is consistent with observations of short-term capacity increase made by [Dührkop et al. \(2017\)](#) and [Buckley et al. \(2020\)](#). As indicated in Figure 14 the beneficial effect of time on shaft resistance is gradually destroyed by continued pile tip penetration.

The preliminary new CRD method is based on piles with  $D/t_w$  ratios of between 16 and 67. A larger database of pile driving records, which includes a range of pile geometries, is required to further develop the method. Figure 20 shows similar back analysis from seven locations at a windfarm in the Southern North Sea that employed monopile foundations driven into chalk. The chalk was exposed from the ground surface at the locations considered; structureless chalk (CIRIA Grade Dm) was underlain by low-medium density structured chalk (Grade A2-B5). The monopiles had diameters of between 4.11 and 4.7 and  $D/t_w$  ratios of 68.5 to 78, exceeding the range used to develop the new CRD method. The piles penetrated under their own weight to depths of between 5 and 12m in the structureless and weathered chalk before being driven to their final depths. Figure 20 (a) and (c) indicate that the method (applied with ratios of  $q_{ba}$  of 0.4 and  $0.6q_{t1.5D}$ , respectively) tends to under-predict the blow counts recorded during monopile penetration, particularly towards the base. The latter suggests that CRD modelling for larger diameter monopiles may benefit from implementing a reduction in the lower limit on  $h/R^*$  (the lower limit of 6 applies within 3m of the final penetration depth, for these monopiles piles with  $R^* \approx 0.5$ ) which controls the response close to the base. The fit between measured and predicted blow counts is improved in this case by reducing the lower limit on  $h/R^*$  to 1 (see Figure 20 (b) and (d)). The calibration of the shaft viscosity parameters may also influence the trends seen in Figure 20.

It is clear that additional data is required to further develop this preliminary model to estimate CRD, particularly for  $D/t_w$  ratios that fall outside the existing database range. Further refinement will be possible as additional datasets become available.

## SUMMARY & CONCLUSIONS

---

- One-dimensional stress wave theory has been successfully applied to consider pile driving in chalk, covering both forward prediction of pile driveability through given strata and back analysis of pile capacity at various stages of driving;
- Low average shaft resistances were observed during driving in chalk, which showed a clear trend to reduce with increasing relative penetration ( $L_p/R^*$ ). Analysis of the dynamic data showed the local shaft resistance falling rapidly with  $h/R^*$ . The relative rates of degradation with  $h/R^*$  observed during pile driving in chalk are far larger than in sands or clays;
- Pile capacity increases were observed in chalk over operational driving pauses which degraded with further hammer blows or pile penetration;
- An approach similar to that adopted previously in sands has been developed to predict local radial effective stresses and short-term shaft resistances during continuous driving in chalk, as a function of local CPT cone resistances, the relative depth,  $h$ , of the pile tip and the interface shearing angle,  $\delta'$ ;
- The approach was developed from signal matching of dynamic monitoring data from piles with diameters between 0.139m and 3.7m ( $D/t_w$  ratios of 16 to 67). The results, obtained using research-oriented soil resistance models, showed a tendency for the rates of degradation with continuous penetration to increase with increasing diameter-to-wall thickness ratio;
- The new proposed CRD prediction method was implemented into a driveability analysis program. Incorporating the site-specific hammer characteristic, actual energy applied and dynamic modelling parameters allowed predictions to be made for well-characterised and independent case histories. The traditional [Smith \(1962\)](#) models were used with a modification to account for the non-linear dependence of strength on velocity. The newly proposed method was shown to give better predictions for continuous driving cases (whose geometries lay within the method calibration space) than the currently applied industrial method for chalk. An adjustment to the model was required to cover larger diameter monopile penetration. Additional cases, particularly at high  $D/t_w$  ratios ( $>67$ ) are required to fully test the model's performance.

- Further development and refinement of the method will be possible as the database of available high-quality dynamic tests is extended by adding test sites with both similar and differing chalk grades and densities. The performance may be improved by further calibration of the rate dependent viscosity parameters in chalk and/or reducing the lower limit on  $h/R^*$ . The method may also be combined with the preliminary Chalk ICP-18 method ([Jardine \*et al.\*, 2018](#)) which aims to predict static long term axial capacity for piles installed in low to medium density chalk.

## Acknowledgements

---

This study was part of a joint industry project led by Pedro Barbosa between Iberdrola, Imperial College and Geotechnical Consulting Group, supported by Innovate-UK. The Authors are grateful to Professor Mark Randolph for the use of IMPACT and also acknowledge the support of Peter Middendorp and Allnamics BV for the use and development of Allwave-PDP. We also acknowledge the offshore wind developer who provided the additional data. The MSc students who contributed to the research (Christopher Norrie, Ignacio Ebensperger and Sarah Norrie) are also gratefully acknowledged.



## REFERENCES

---

- Allnamics (2015). *AllWavePDP User's reference manual*, Allnamics BV, Draft for review and comment.
- Alm T. & Hamre, L. (2002). Soil model for pile driveability predictions based on CPT interpretations. *Proc. 15th Intl. Conf. Soil Mech. Geotech. Eng.*, Istanbul, Turkey: 1297-1302.
- Alves A. M., Lopes, F. R., Randolph, M. F. & Danziger, B. R. (2009). Investigations on the dynamic behavior of a small-diameter pile driven in soft clay. *Can. Geotech. J.*, **46**, No. 12: 1418-1430.
- Barbosa P., Geduhn, M., Jardine, R. J., Schroeder, F. C. & Horn, M. (2015). Offshore pile load tests in chalk. *Proc. 16th Eur. Conf. Soil Mech. Geotech. Eng.*, Edinburgh, Scotland: 2885-2890.
- Biscontin G. & Pestana, J. M. (2001). Influence of peripheral velocity on vane shear strength of an artificial clay. *Geotechnical Testing Journal*, **24**, No. 4: 423-429.
- Bowden A. J., Spink, T. W. & Mortimore, R. N. (2002). The engineering description of chalk: its strength, hardness and density. *Q. J. Eng. Geol. Hydrogeol.*, **35**, No. 4: 355-361.
- Bristow C. R., CR, B., RA, B., RW, G. & ER, S. T. (1972). *Geology of the country around Royal Tunbridge Wells*. No.:
- Brown M. J. & Hyde, A. F. L. (2008). Rate effects from pile shaft resistance measurements. *Canadian Geotechnical Journal*, **45**, No. 3: 425-431.
- Brown M. J. & Powell, J. J. (2013). Comparison of rapid load test analysis techniques in clay soils. *Journal of geotechnical and geoenvironmental engineering*, **139**, No. 1: 152-161.
- Buckley R. M. (2018). *The axial behaviour of displacement piles in chalk*. PhD Thesis, Imperial College London, London, UK.
- Buckley R. M., Jardine, R. J., Kontoe, S., Barbosa, P. & Schroeder, F. C. (2020). Full-scale observations of dynamic and static axial responses of offshore piles driven in chalk and tills, *Géotechnique*, online ahead of print. <https://doi.org/10.1680/jgeot.19.TI.001>.
- Buckley R. M., Jardine, R. J., Kontoe, S. & Lehan, B. M. (2018a). Effective stress regime around a jacked steel pile during installation ageing and load testing in chalk. *Can. Geotech. J.*, **55**, No. 11: 1577-1591.
- Buckley R. M., Jardine, R. J., Kontoe, S., Parker, D. & Schroeder, F. C. (2018b). Ageing and cyclic behaviour of axially loaded piles driven in chalk. *Géotechnique*, **68**, No. 2: 146-161.
- Buckley R. M., Kontoe, S., Jardine, R. J., Maron, M., Schroeder, F. C. & Barbosa, P. (2017). Common pitfalls of pile driving resistance analysis - A case study of the Wiking offshore windfarm. *Proc. 8th Intl. Conf. Offshore Site Investigation and Geotechnics*, London, UK: 1246-1253.
- Byrne T., Doherty, P., Gavin, K. & Overy, R. (2012). Comparison of Pile Driveability Methods In North Sea Sand. *Proc. 7th Intl Conf. Offshore Site Investigations and Geotechnics*, London, UK: 481-488.
- Carotenuto P., Meyer, V., Strøm, P. J., Cabarkapa, Z., St. John, H. & Jardine, R. J. (2018). Installation and axial capacity of the Sheringham Shoal offshore wind farm monopiles – a case history. *Engineering in Chalk*, London, UK: 117-122.
- Chan L. D., Buckley, R. M., Liu, T. & Jardine, R. J. (2019). Laboratory investigation of interface shearing in chalk. *Proc. 7th International Symposium on Deformation Characteristics of Geomaterials*, Glasgow, UK: 1-6.
- Chow F. C. (1997). *Investigations into Displacement Pile Behaviour for Offshore Foundations*. PhD Thesis, Imperial College London, London, UK.

- Ciavaglia F., Carey, J. & Diambra, A. (2017). Time-dependent uplift capacity of driven piles in low to medium density chalk. *Géotechnique Letters*, **7**, No. March: 1-7.
- Coyle H. M. & Gibson, G. C. (1970). Empirical damping constants for sands and clays. *J. Soil Mech. Found. Div. - ASCE*, **96**, No. 3: 949-965.
- Dayal U. & Allen, J. H. (1975). The effect of penetration rate on the strength of remolded clay and sand samples. *Can. Geotech. J.*, **12**, No. 3: 336-348.
- De Josselin de Jong G. (1956). Wat gebeurt er in de grond tijdens het heien. *De Ingenieur*, **68**, No.: B77-B88.
- Deeks A. J. & Randolph, M. F. (1991). Evaluation of the inelastic response of an axisymmetric foundation to impact loading. *Proc. 7th Intl. Conf. on Computer Methods and Advances in Geomechanics*, Cairns, Australia: 735-740.
- Deeks A. J. & Randolph, M. F. (1995). A simple model for inelastic footing response to transient loading. *Int. J. Num. Meth. Geotech. Eng.*, **19**, No. 5: 307-329.
- Doughty L. J., Buckley, R. M. & Jardine, R. J. (2018). Investigating the effect of ageing on the behaviour of chalk putty. *Engineering in Chalk*, London, UK: 695-701.
- Dührkop J., Maretzki, S. & Rieser, J. (2017). Re-evaluation of pile driveability in chalk. *Proc. 8th Intl. Conf. Offshore Site Investigation and Geotechnics* London, UK: 666-673.
- Ebensperger I. (2017). *Back Analysis of Offshore Pile Driving Records in Chalk and Glacial Till*. MSc. Thesis, Imperial College London, London, UK.
- Esper S. (2017). *Back analysis of offshore pile driving records in chalk*. MSc Thesis, Imperial College London, London, UK.
- Fellenius B. H. (1988). Variation of CAPWAP results as a function of the operator. *Proc. 3rd Intl. Conf. on the Application of Stress Wave Theory to Piles*, Ottawa, Canada: 814-825.
- Fugro (2013). *Wikingen Offshore Windfarm: Advanced Laboratory and Drivability Assessment*, Fugro Geoconsulting Ltd., J22026-1.
- Gavin K. & Lehane, B. M. (2007). Base load-displacement response of piles in sand. *Can. Geotech. J.*, **44**, No. 9: 1053-1063.
- Han F., Ganju, E., Prezzi, M., Salgado, R. & Zaheer, M. (2019). Axial resistance of open-ended pipe pile driven in gravelly sand. *Géotechnique*, <https://doi.org/10.1680/jgeot.18.P.117>, No.:
- Heerema E. P. (1978). Predicting pile driveability: heather as an illustration of the friction fatigue theory. *Proc. Eur. Offshore Petroleum Conf.*, London, UK: 413-422.
- Holeyman A. (1985). Dynamic non-linear skin friction of piles. *Proc. Intl. Symp. on penetrability and driveability of piles - technical committee on penetrability and drivability of piles.*, San Francisco, California: 173-176.
- Jardine R. J., Buckley, R. M., Kontoe, S., Barbosa, P. & Schroeder, F. C. (2018). Behaviour of piles driven in chalk. *Engineering in Chalk*, London, UK: 33-51.
- Jardine R. J., Chow, F. C., Overy, R. & Standing, J. R. (2005). *ICP design methods for driven piles in sands and clays*, London: Thomas Telford.
- Le T. M. H., Eiksund, G. R. & Strøm, P. J. (2014). Characterisation of Residual Shear Strength at the Sheringham Shoal Offshore Wind Farm. *Proc. 33rd Intl. Conf. Ocean, Offshore and Arctic Eng.*, San Francisco, California: 1-9.
- Lee S. L., Chow, Y. K., Karunaratne, G. P. & Wong, K. Y. (1988). Rational wave equation model for pile-driving analysis. *J. Geotech. Eng. - ASCE*, **114**, No. 3: 306-325.
- Lehane B. M., Jardine, R. J., Bond, A. J. & Frank, R. (1993). Mechanisms of shaft friction in sand from instrumented pile tests. *J. Geotech. Eng - ASCE*, **119**, No. 1: 19-35.

- Lehane B. M., Schneider, J. A. & Xu, X. (2005). The UWA-05 method for prediction of axial capacity of driven piles in sand. *Proc. 1st Intl. Symp. Frontiers in Offshore Geotechnics*, Perth, Australia: 683-689.
- Litkouthi S. & Poskitt, T. J. (1980). Damping constants for pile driveability calculations. *Géotechnique*, **30**, No. 1: 77-86.
- Lord J. A., Clayton, C. R. I. & Mortimore, R. N. (2002). *Engineering in chalk*, CIRIA, C574.
- Loukidis D., Salgado, R. & Abou-Jaoude, G. (2008). *Assessment of Axially-Loaded Pile Dynamic Design Methods and Review of INDOT Axially-Loaded Design Procedure*, Purdue University, FHWA, FHWA/IN/JTRP-2008/6.
- Lysmer J. & Richart, F. E. (1966). Dynamic response of footings to vertical loading. *J. Eng. Mech. Div. - ASCE*, **92**, No. 1: 65-91.
- Matthews M. C. & Clayton, C. R. I. (1993). Influence of intact porosity on the engineering properties of a weak rock. *Intl. Symp. Geotechnical Engineering of Hard Soils and Soft Rocks*, Rotterdam, the Netherlands: 693-702.
- Middendorp P. (2016). *AllWave-PDP Buckley fatigue model instructions - Personal Communication*.
- Norrie C. (2015). *Pile driving performance in low to medium density chalk*. MSc Thesis, Imperial College London, London, UK.
- Randolph M. F. (1987). Modelling of the soil plug response during pile driving. *Proc. 9th South East Asian Conf. Soil Mech.*, Bangkok, Thailand: 6.1-6.14.
- Randolph M. F. (1993). Analysis of stress-wave data from pile tests at Pentre and Tilbrook. *Large-scale pile tests in clay*, 1993 London. pp.
- Randolph M. F. (2008). *IMPACT - Dynamic analysis of pile driving*, Manual.
- Randolph M. F. & Simons, H. A. (1986). An improved soil model for one-dimensional pile driving analysis. *Proc. 3rd Intl. Conf. Numerical Methods in Offshore Piling*, Nantes, France: 3-17.
- Rausche F., Moses, F. & Goble, G. G. (1972). Soil resistance predictions from pile dynamics. *Journal of the Soil Mechanics and Foundations Division*, **98**, No. 9: 917-937.
- Rimoy S. P., Silva, M., Jardine, R. J., Yang, Z. X., Zhu, B. T. & Tsuha, C. H. C. (2015). Field and model investigations into the influence of age on axial capacity of displacement piles in silica sands. *Géotechnique*, **65**, No. 7: 576-589.
- Salgado R., Loukidis, D., Abou-Jaoude, G. & Zhang, Y. (2015). The role of soil stiffness non-linearity in 1D pile driving simulations. *Géotechnique*, **65**, No. 3: 169-187.
- Schneider J. A. & Harmon, I. A. (2010). Analyzing Drivability of Open Ended Piles in Very Dense Sands. *DFI Journal*, **4**, No. 1: 32-44.
- Simons H. A. & Randolph, M. F. (1985). A new approach to one dimensional pile driving analysis. *Intl. Conf. on Numerical Methods in Geomechanics*, Nagoya, Japan: 1457-1464.
- Smith A. K. C. (2001). Interpretation of cone penetration tests in chalk. *Ground Engineering*, **34**, No. 9: 30-35.
- Smith E. A. L. (1962). Pile-driving analysis by the wave equation. *J. Soil Mech Found. Eng. - ASCE*, **4**, No. 86: 35-61.
- Stevens R. S., Wiltsie, E. A. & Turton, T. H. (1982). Evaluating drivability for hard clay very dense sand and rock. *Offshore Technology Conference*, 1982 Houston, Texas. pp 465-483.
- Toolan F. E. & Fox, D. A. (1977). Geotechnical planning of piled foundations for offshore platforms. *Proc of the ICE - Civil Engineering*, **62**, No. 2: 221-244.
- Triantafyllidis T. (2001). On the application of the Hiley formula in driving long piles. *Geotechnique*, **51**, No. 10: 891-895.

Ziogos A., Brown, M., Ivanovic, A. & Morgan, N. (2017). Chalk-steel interface testing for marine energy foundations. *Proc. of the ICE Geotech. Eng*, **170**, No. 3: 285-298.

## NOTATION

---

### Roman Alphabet

$A_{ann}$	Cross-sectional area of the open-ended pile annulus
$C_b$	Base dashpot constant (dynamic soil resistance models)
$c_s$	Shaft dashpot constant (dynamic soil resistance models)
$D$	Diameter of pile
$F$	Force at the pile head (PDA)
$F_{up}$	Upward travelling component of force
$f_s$	CPTu sleeve friction
$G$	Shear modulus
$G_{max}$	Maximum shear modulus
$G_1$	Secant shear modulus
$h$	Distance from the pile tip
$J_s$	Smith damping constant (shaft)
$J'_s$	Smith damping constant (shaft) allowing for viscous effects
$K_b$	Base spring constant (dynamic soil resistance models)
$k_s$	Shaft spring constant (dynamic soil resistance models)
$L_p$	Length of pile penetration
$L_{p,chk}$	Length of pile penetration in chalk
$m_0$	Supplementary lumped mass connected through pile base node
$m_1$	Supplementary lumped mass connected through pile radiation dashpot
$p'$	Mean effective stress
$p_a$	Atmospheric pressure
$Q_b$	Pile base axial load resistance (capacity)
$q_{ba}$	Pile end-bearing resistance under annulus
$q_{b,stat}$	Limit base stress plastic slider (dynamic soil resistance model)
$q_t$	Net (corrected) cone resistance
$q_{t,1.5D}$	Average net CPT tip resistance $\pm 1.5D$ around pile base
$q_u$	Unconfined compressive strength
$R$	Pile radius
$R_a$	Average centre line roughness
$R^*$	Equivalent radius for open-ended piles
$R_i$	Internal pile radius
$s_u$	Undrained shear strength
$t$	time
$t_w$	Pile wall thickness
$U_{q,s}$	Shaft loading quake (dynamic soil resistance model)
$U_{q,b}$	Base loading quake (dynamic soil resistance model)
$u_1$	PCPT excess pore water pressures measured at the tip position
$u_2$	PCPT excess pore water pressures measured at the shoulder position

$V_s$	Elastic shear wave velocity
$v$	Velocity or specific volume
$v_0$	Reference velocity (1m/s)
$w$	Displacement
$Z$	Pile impedance
$z$	Depth

### **Greek alphabet**

$\alpha_s$	Shaft viscosity parameter (soil resistance model)
$\beta_s$	Shaft viscosity parameter (soil resistance model)
$\Delta v$	Relative velocity between the pile and soil
$\delta'_{ult}$	Ultimate interface angle of shearing resistance
$\zeta$	Multiplier for radial effective stress expression
$\eta$	Exponent for radial effective stress expression
$\lambda$	Slope of the isotropic compression line
$N$	Specific volume on the NCL at $p'=1\text{kPa}$
$\rho_s$	Soil or chalk mass density
$\sigma'_{ri}$	Radial effective stress during installation
$\sigma'_{v0}$	Vertical effective yield stress
$\tau$	Shaft shear stress
$\tau_{avg}$	Average shaft shear stress at failure from static or dynamic test
$\tau_{fi}$	Calculated local shear stress during driving (SRD)
$\tau_{inter}$	Limit shaft resistance in the pile-soil interface (dynamic soil resistance model)
$\tau_s$	Static shaft resistance
$\tau_{s,d}$	Local shear stress at failure interpreted from dynamic tests
$\tau_{s,p}$	Local shear stress calculated using soil disp and pile velocity (dynamic soil resistance model)
$\nu$	Poisson's ratio
$\phi'_{cv}$	Angle of shearing resistance at critical state

### **Acronyms & Abbreviations**

BOR	Beginning of restrike
CIRIA	Construction industry research and information association
CPT	Cone penetration resistance
CRD	Chalk resistance to driving
CSL	Critical state line
D	Pile diameter
EOD	End of driving
ICP	Imperial College Pile

ICP-05	Imperial College Pile design method ( <a href="#">Jardine <i>et al.</i>, 2005</a> )
IDD	Intact dry density
NE	North East
NCL	Normal compression line
OD	Outside diameter
OSS	Offshore substation
OWF	Offshore windfarm
SNW	St. Nicholas-at-Wade
SPT	Standard penetration test
SRD	Soil resistance to driving
UCS	Unconfined compressive strength
UK	United Kindom
UWA-05	University of Western Australia axial design method for sands ( <a href="#">Lehane <i>et al.</i>, 2005</a> )
WK	Wikinger offshore wind turbine location
Z <sub>v</sub>	Velocity times impedance

## LIST OF FIGURES

---

Figure 1: Schematic of wave propagation and example measured data during pile driving (a) signal matching on piles monitored with strain gauges and accelerometers during installation (displacement, obtained by double integration of the measured accelerations) (b) back analysis of pile driveability with driving energy and blow count monitoring only

Figure 2: Illustration of stress states during installation, equalisation and ageing of driven piles (after Buckley, 2018)

Figure 3: Distribution of Chalk beneath NW Europe, after Mortimore (2016) also showing Wikingen and St Nicholas at Wade test site locations. Wealdon deposits (Bristow et al., 1972) are not encountered at the test site

Figure 4 Typical cone resistance, sleeve friction and excess pore pressure profiles at Wikingen in Holocene deposits, glacial till and structured/structureless chalk

Figure 5 Typical profiles of cone resistance,  $q_t$ , sleeve friction,  $f_s$ , pore pressure at the sleeve position,  $u_2$  and  $u_1$  measured in PCPT4 or PCPT6 at the Imperial College test site ( $u_1$  pore pressures were measured during PCPT6)

Figure 6 Traditional soil resistance models adapted from Smith (1962)

Figure 7 Rational soil resistance models adopted at the shaft and at the base; adapted from Randolph and Simons (1986) and Deeks and Randolph (1991)

Figure 8: Example signal match from blow at Wikingen: measured and calculated (a) force and velocity times impedance (b) upward travelling force and displacement

Figure 9: Pile velocities integrated from acceleration measurements at the pile head

Figure 10: Displacements at a pile element during a hammer blow for a low resistance driving case

Figure 11 Displacements at a pile element during a hammer blow for a high resistance driving case

Figure 12: Effect of (a) varying  $\beta_s$  on upward travelling wave (b) varying  $\beta_s$  on pile head displacement (c) varying  $\alpha_s$  on upward travelling wave (d) varying  $\alpha_s$  on pile head displacement

Figure 13: Demonstration of change in  $F_{up}$  traces with time over (a) the period between end of driving and beginning of restrike and (b) a pause in pile driving

Figure 14: Change in shaft resistance immediately following a driving pause and with subsequent driving

Figure 15: Effect of continued pile penetration on local shaft resistance obtained from signal matching of individual blows during driving

Figure 16: Trend of normalised radial effective stress reduction with normalised distance from the pile tip for 14 driving blows in chalk

Figure 17: (a) normalised radial effective stresses versus  $h/R^*$  at end of driving for Wikingen 1.37m diameter piles, Wikingen 2.7 to 3.67m diameter piles and SNW 0.139m diameter piles (b) relationship between parameter  $\eta$  and diameter to wall thickness ratio

Figure 18: Measured and calculated with the proposed profiles of shaft resistance at EoD



Figure 19: Back calculated blow count profiles using new driveability method for (a) Wiking 2.7m diameter pile WK69-E(b) Wiking 2.7m diameter pile WK69-S (c) Wiking 1.37m diameter pile WK43-3

Figure 20: Back calculated blow count profiles using new driveability method for seven monopiles at an offshore windfarm in the Southern North Sea for (a)  $q_{ba}=0.4q_t$   $h/R^*\geq 6$  (b)  $q_{ba}=0.4q_t$   $h/R^*\geq 1$  (c)  $q_{ba}=0.6q_t$   $h/R^*\geq 6$  (c)  $q_{ba}=0.6q_t$   $h/R^*\geq 1$

## FIGURES

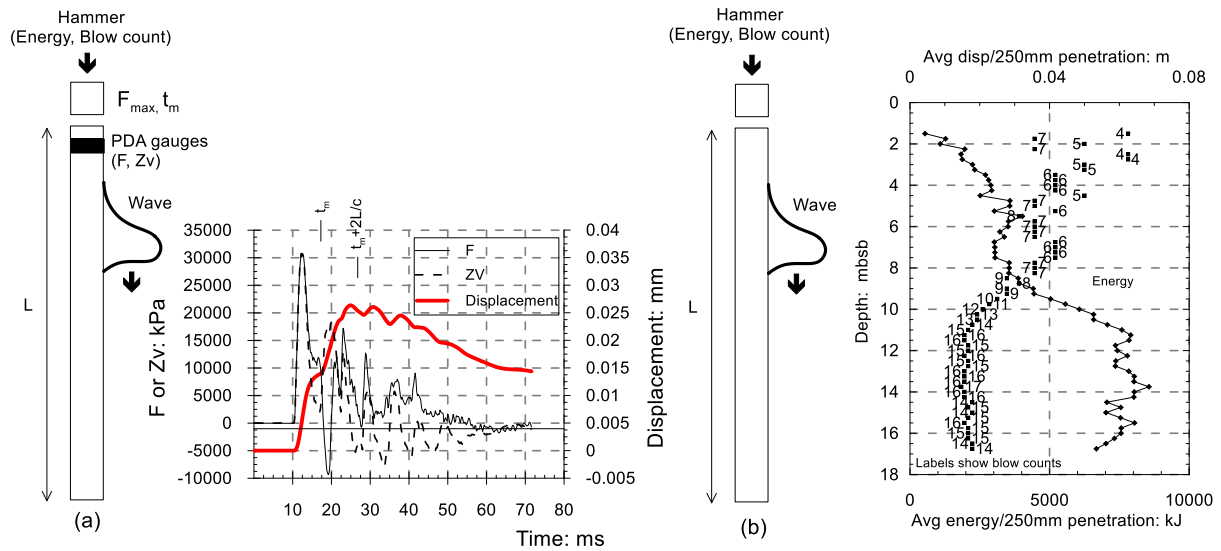


Figure 1: Schematic of wave propagation and example measured data during pile driving (a) signal matching on piles monitored with strain gauges and accelerometers during installation (displacement, obtained by double integration of the measured accelerations) (b) back analysis of pile driveability with driving energy and blow count monitoring only

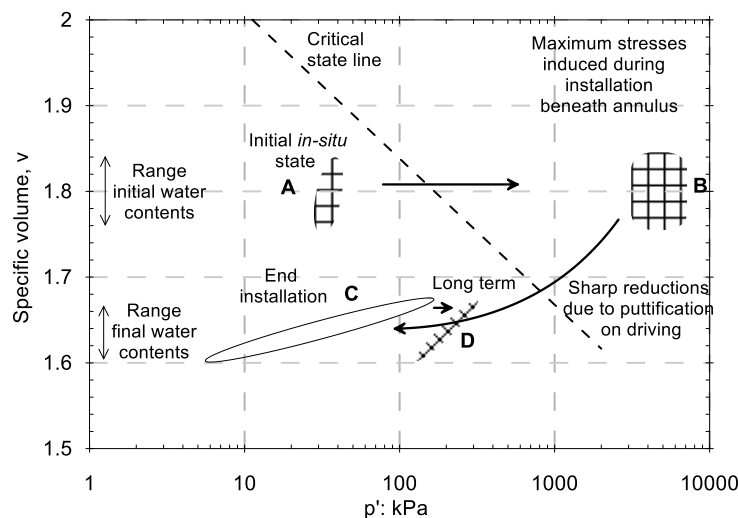


Figure 2: Illustration of stress states during installation, equalisation and ageing of driven piles (after Buckley, 2018)

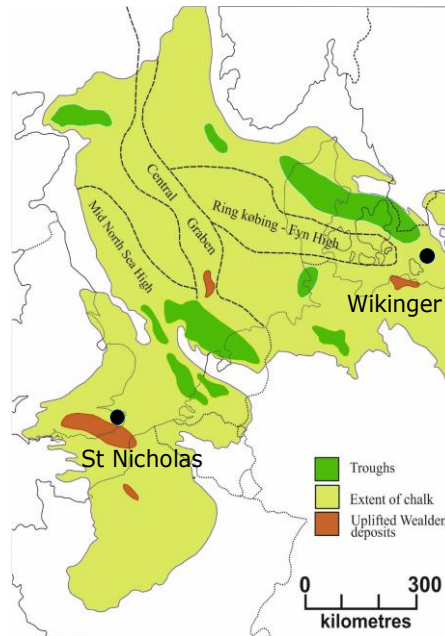


Figure 3: Distribution of Chalk beneath NW Europe, after Mortimore (2016) also showing Wikinger and St Nicholas at Wade test site locations. Wealdon deposits (Bristow et al., 1972) are not encountered at the test site

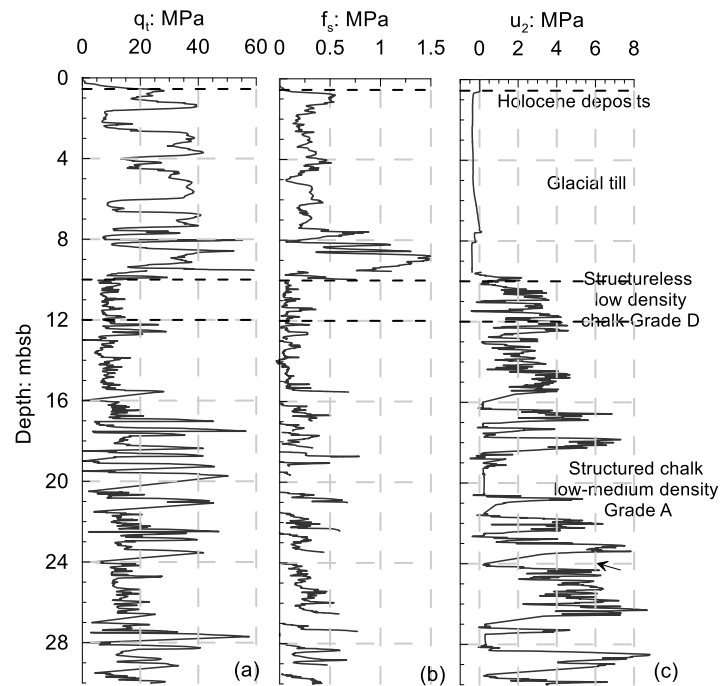


Figure 4 Typical cone resistance, sleeve friction and excess pore pressure profiles at Wikinger in Holocene deposits, glacial till and structured/structureless chalk

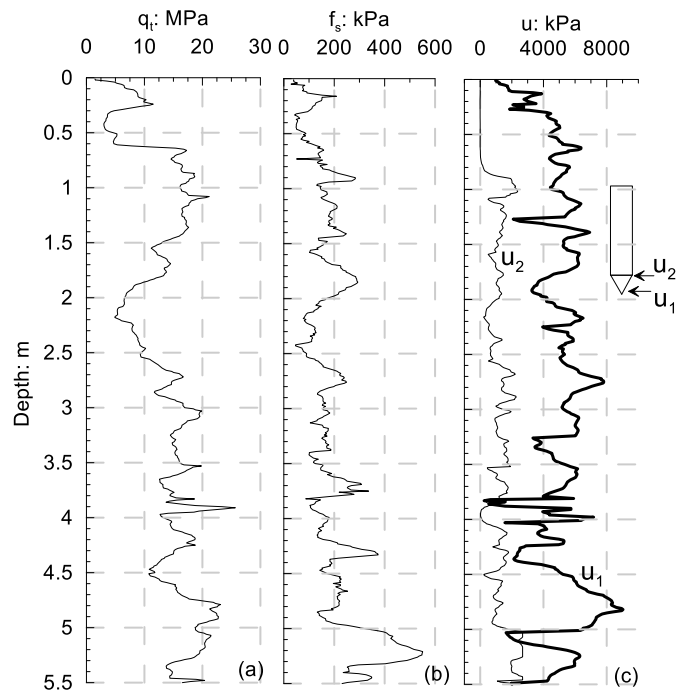


Figure 5 Typical profiles of cone resistance,  $q_r$ , sleeve friction,  $f_s$ , pore pressure at the sleeve position,  $u_2$  and  $u_1$  measured in PCPT4 or PCPT6 at the Imperial College test site ( $u_1$  pore pressures were measured during PCPT6)

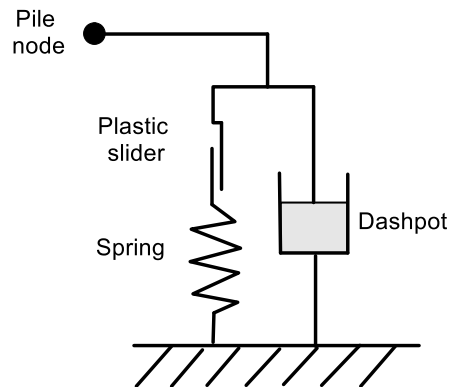


Figure 6 Traditional soil resistance models adapted from [Smith \(1962\)](#)

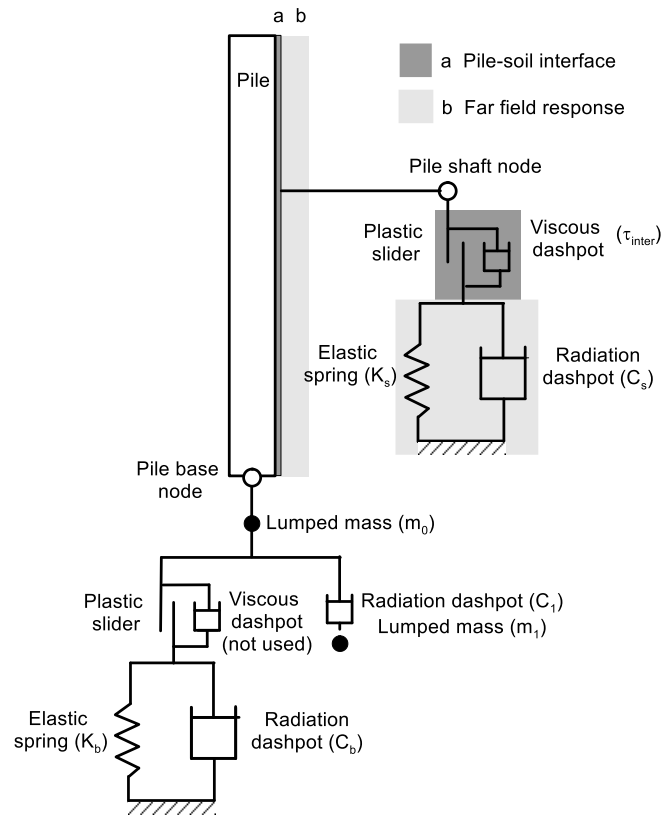


Figure 7 Rational soil resistance models adopted at the shaft and at the base; adapted from [Randolph and Simons \(1986\)](#) and [Deeks and Randolph \(1991\)](#)

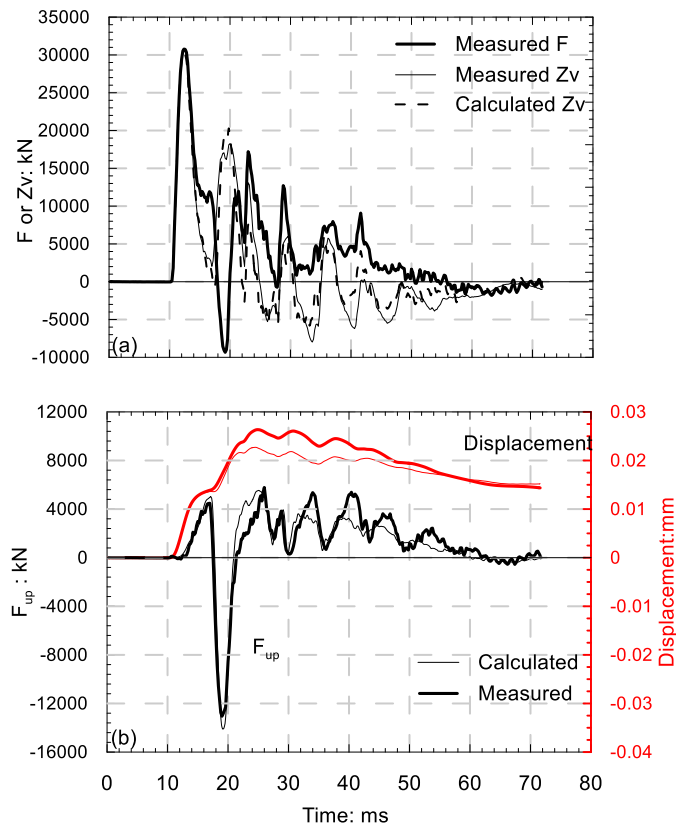


Figure 8: Example signal match from blow at Wikinger: measured and calculated (a) force and velocity times impedance (b) upward travelling force and displacement

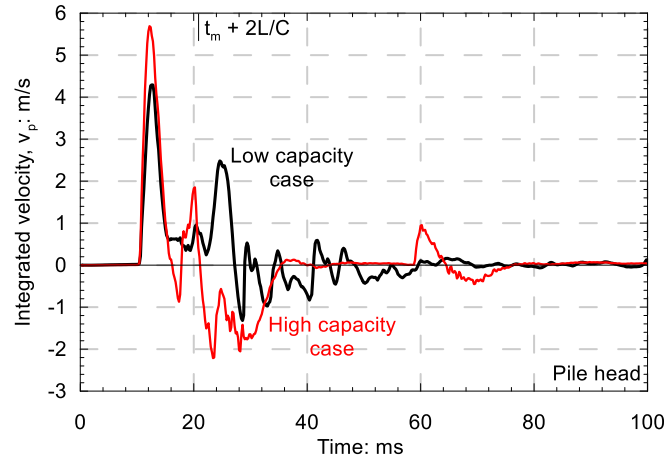


Figure 9: Pile velocities integrated from acceleration measurements at the pile head

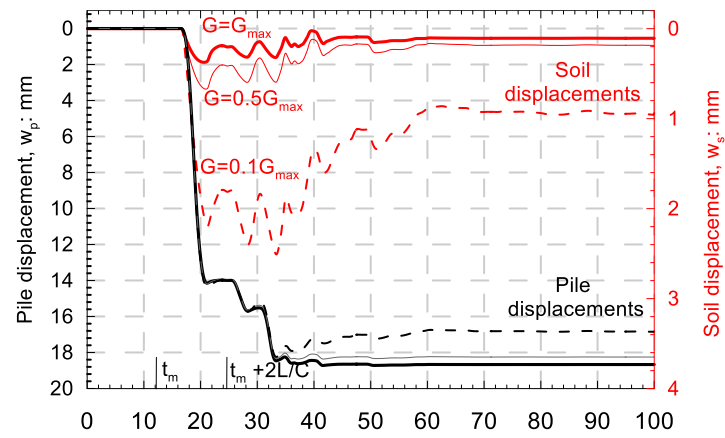


Figure 10: Displacements at a pile element during a hammer blow for a low resistance driving case

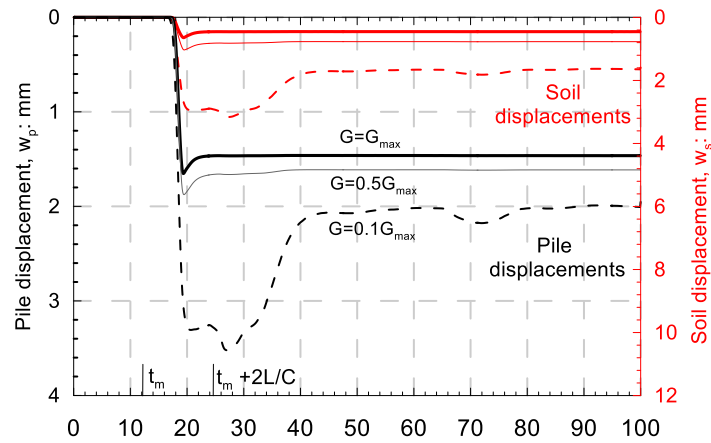


Figure 11 Displacements at a pile element during a hammer blow for a high resistance driving case

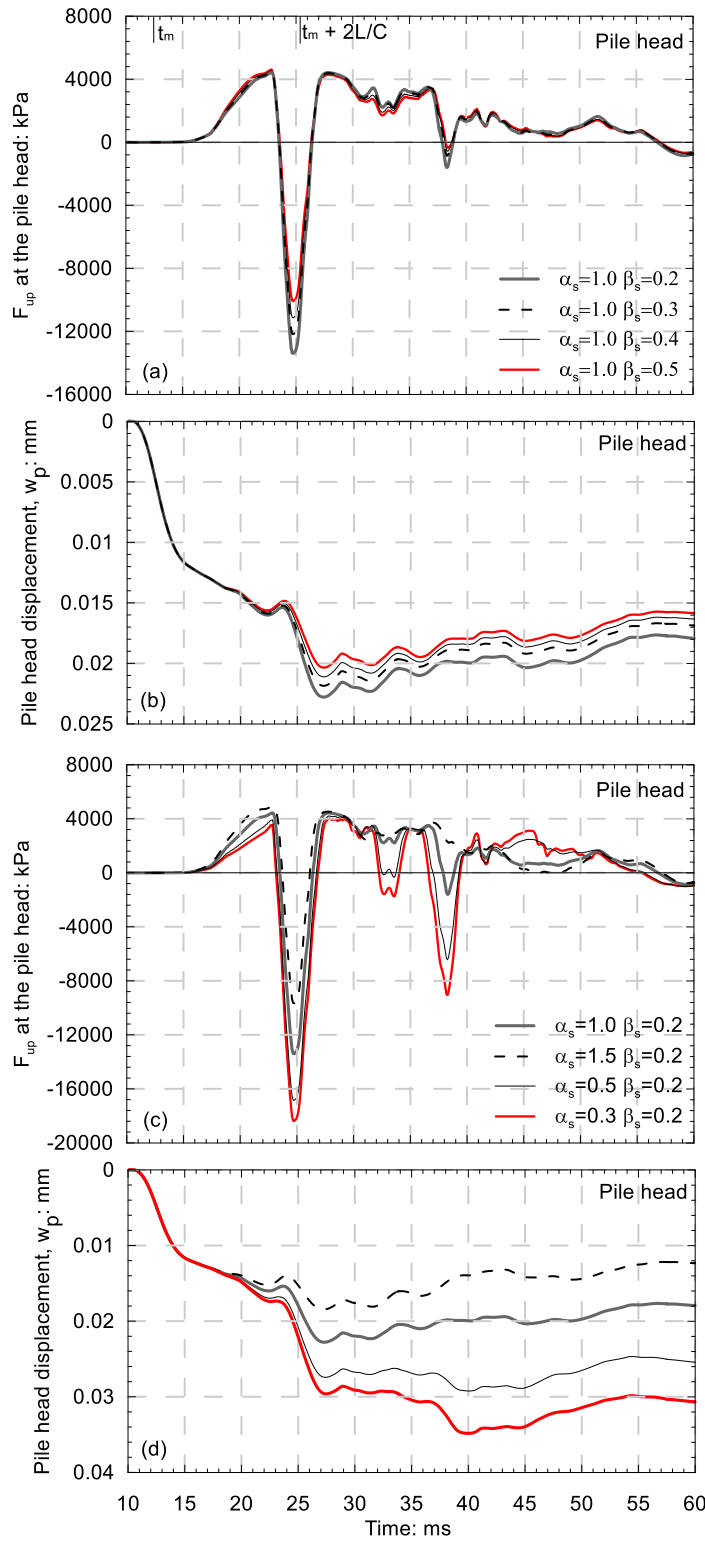


Figure 12: Effect of (a) varying  $\beta_s$  on upward travelling wave (b) varying  $\beta_s$  on pile head displacement (c) varying  $\alpha_s$  on upward travelling wave (d) varying  $\alpha_s$  on pile head displacement

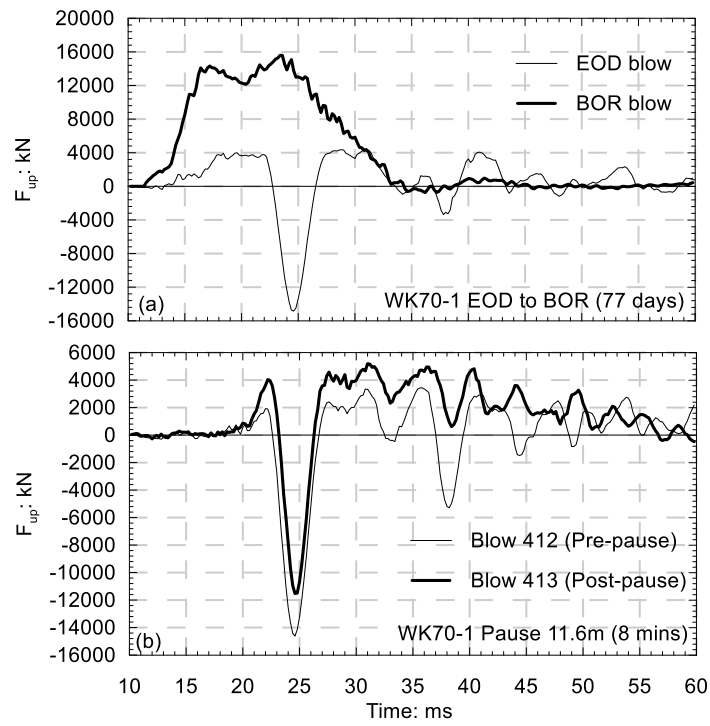


Figure 13: Demonstration of change in  $F_{up}$  traces with time over (a) the period between end of driving and beginning of restrike and (b) a pause in pile driving

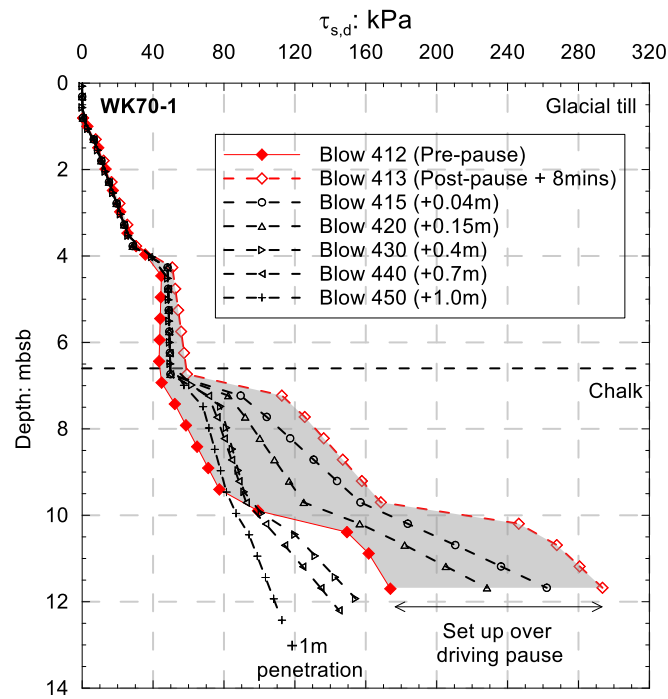


Figure 14: Change in shaft resistance immediately following a driving pause and with subsequent driving

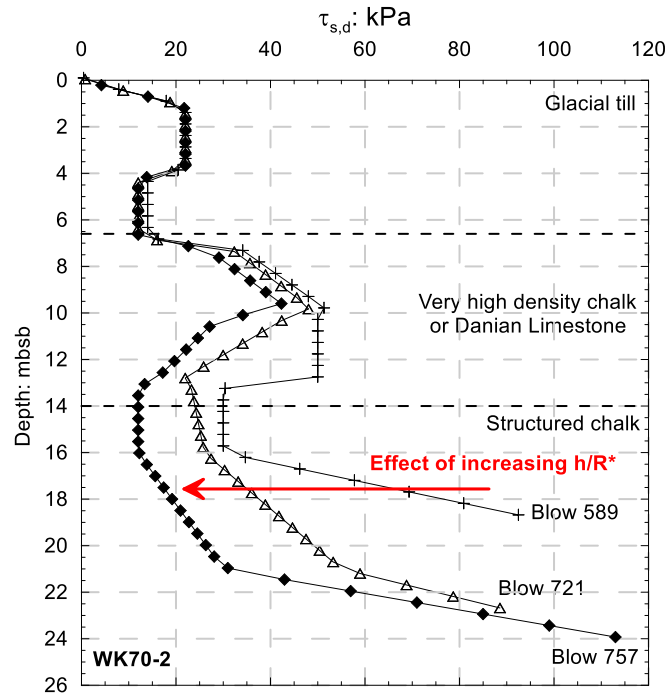


Figure 15: Effect of continued pile penetration on local shaft resistance obtained from signal matching of individual blows during driving

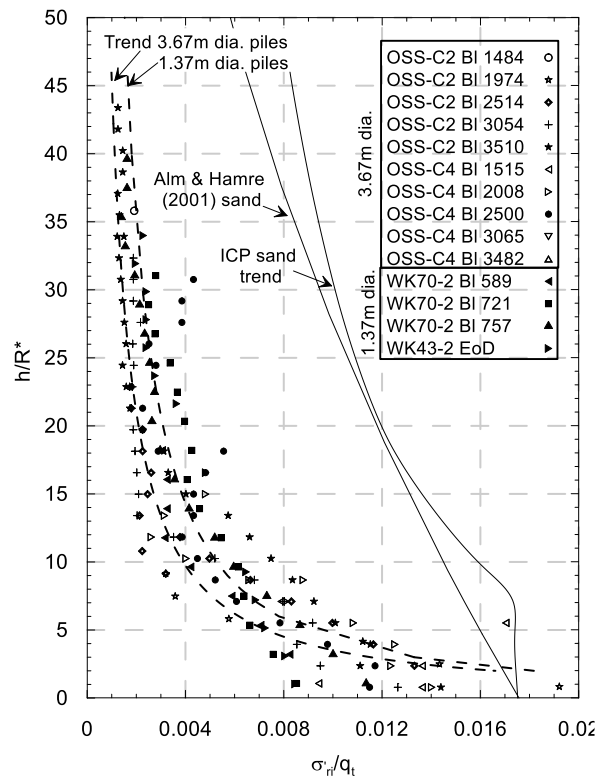


Figure 16: Trend of normalised radial effective stress reduction with normalised distance from the pile tip for 14 driving blows in chalk



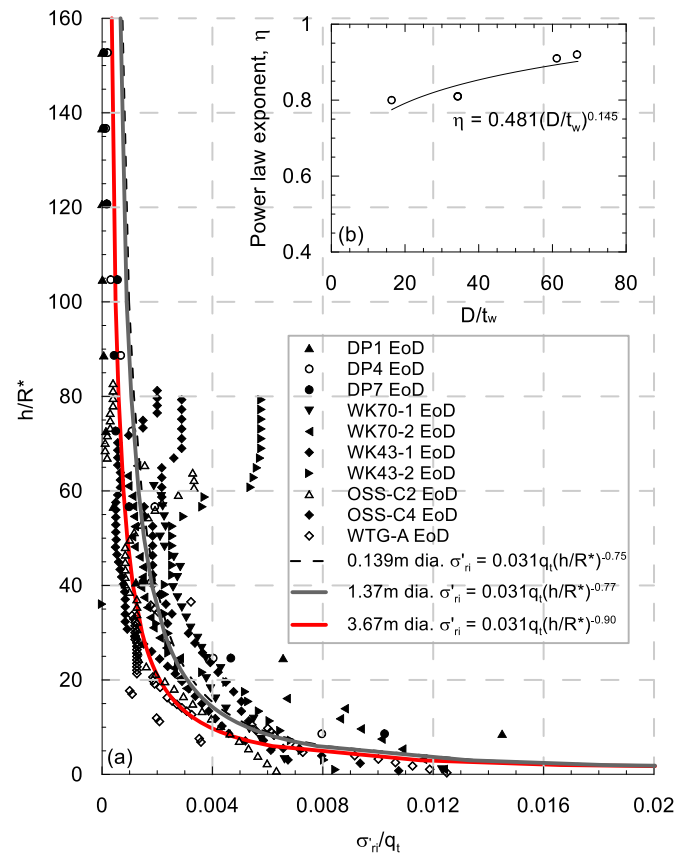


Figure 17: (a) normalised radial effective stresses versus  $h/R^*$  at end of driving for Wikinger 1.37m diameter piles, Wikinger 2.7 to 3.67m diameter piles and SNW 0.139m diameter piles (b) relationship between parameter  $\eta$  and diameter to wall thickness ratio

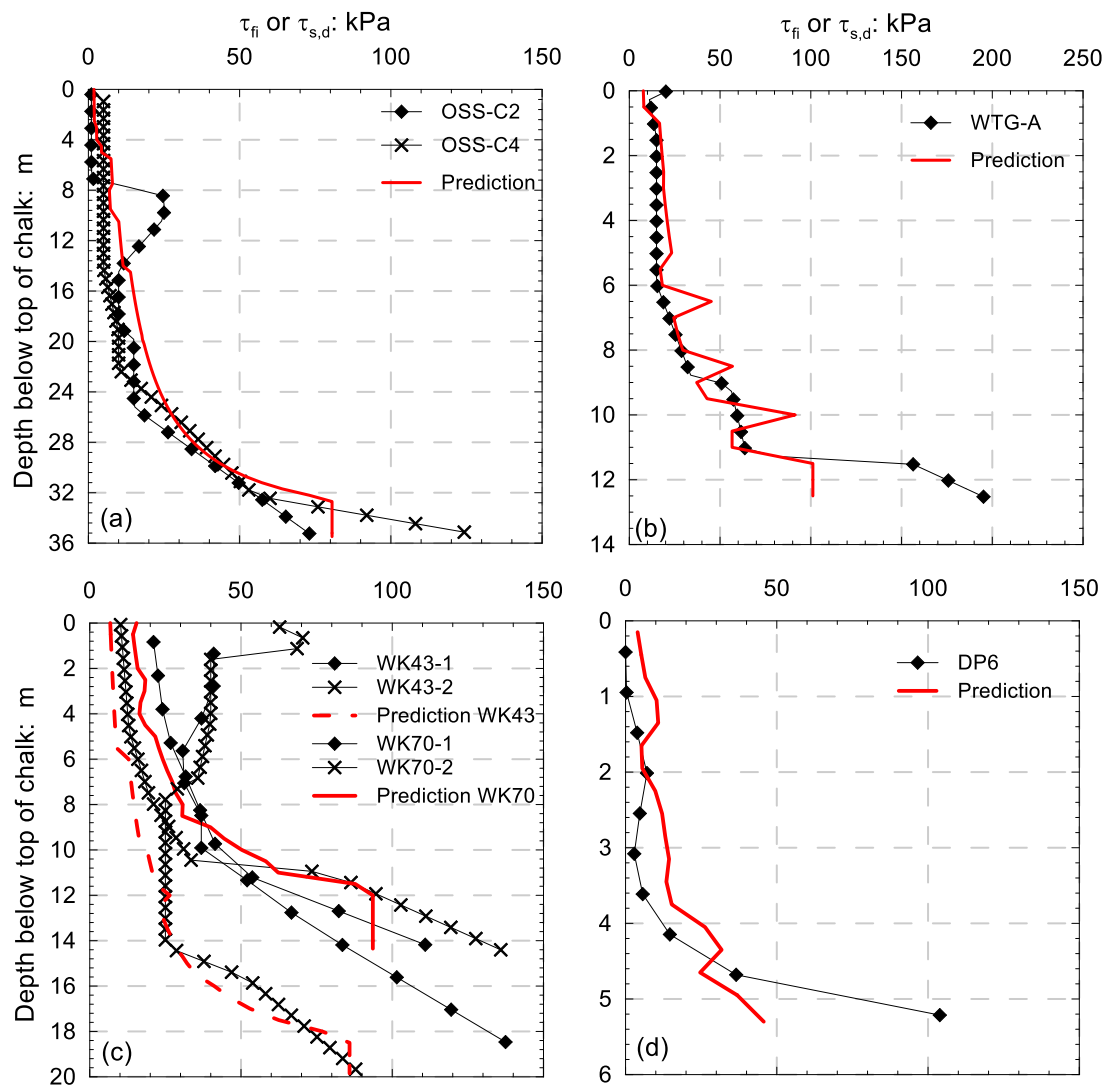


Figure 18: Measured and calculated with the proposed profiles of shaft resistance at EoD

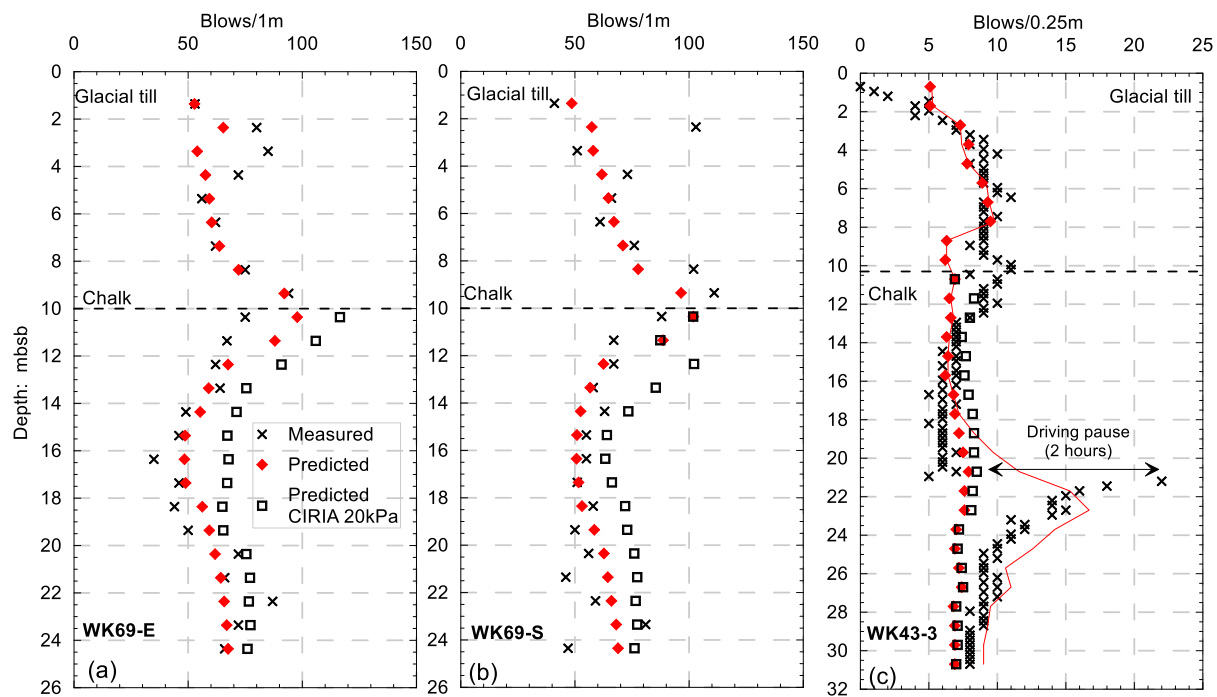


Figure 19: Back calculated blow count profiles using new driveability method for (a) Wikinger 2.7m diameter pile WK69-E (b) Wikinger 2.7m diameter pile WK69-S (c) Wikinger 1.37m diameter pile WK43-3

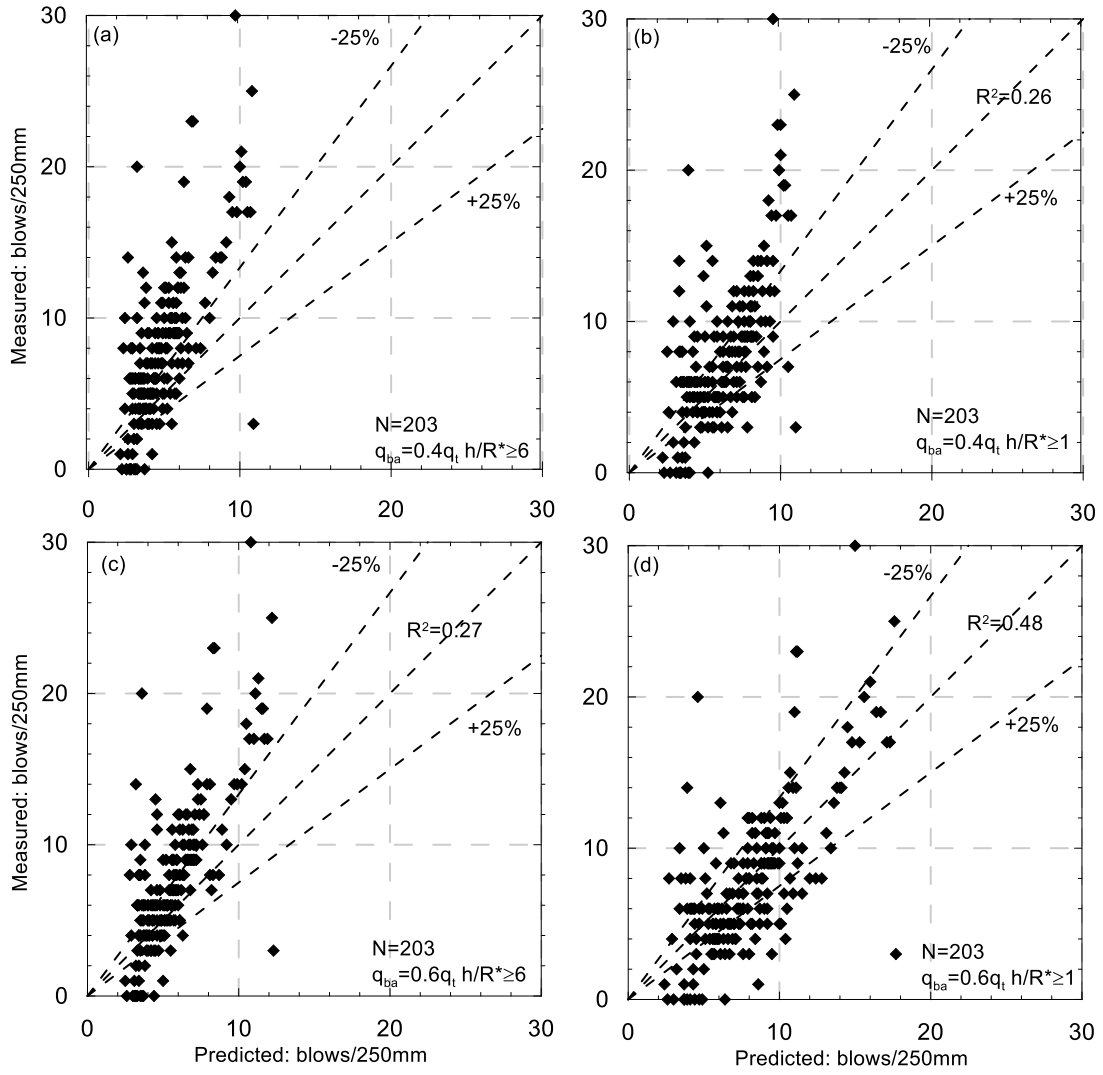


Figure 20: Back calculated blow count profiles using new driveability method for seven monopiles at an offshore windfarm in the Southern North Sea for (a)  $q_{ba}=0.4q_t$ ,  $h/R^*\geq 6$  (b)  $q_{ba}=0.4q_t$ ,  $h/R^*\geq 1$  (c)  $q_{ba}=0.6q_t$ ,  $h/R^*\geq 6$  (d)  $q_{ba}=0.6q_t$ ,  $h/R^*\geq 1$